Structural Complexity of Glyphosate and Aminomethylphosphonate Metal Complexes

Olivia Rusli, [a] Oscar H Lloyd Williams,[a] Papri Chakraborty,[b] Marco Neumaier,[b] Frank Hennrich,[c] Sjors Bakels,[d] Kevin Hes,[d] Anouk M Rijs,[d] Boris Ucur,[e] Shane R Ellis,[e] River J Pachulicz,[f] Tara L Pukala,[f] and Nicole J Rijs*[a]

[a.] *School of Chemistry, UNSW Sydney, Sydney, NSW, 2052, Australia*
[b.] *Institute of Nanotechnology, Karlsruhe Institute of Technology, 76344 Eggenstein-Leopoldshafen, Germany*
[c.] *Institute of Quantum Materials and Technologies, Karlsruhe Institute of Technology, 76021 Karlsruhe, Germany*
[d.] *Division of BioAnalytical Chemistry, Department of Chemistry and Pharmaceutical Sciences, Vrije Universiteit Amsterdam, The Netherlands*
[e.] *Molecular Horizons and School of Chemistry and Molecular Bioscience, University of Wollongong, NSW, 2522, Australia*
[f.] *Department of Chemistry, School of Physics, Chemistry and Earth Sciences, The University of Adelaide, Australia*

Supplementary Information

Table of Contents

Experimental

Experimental Workflow

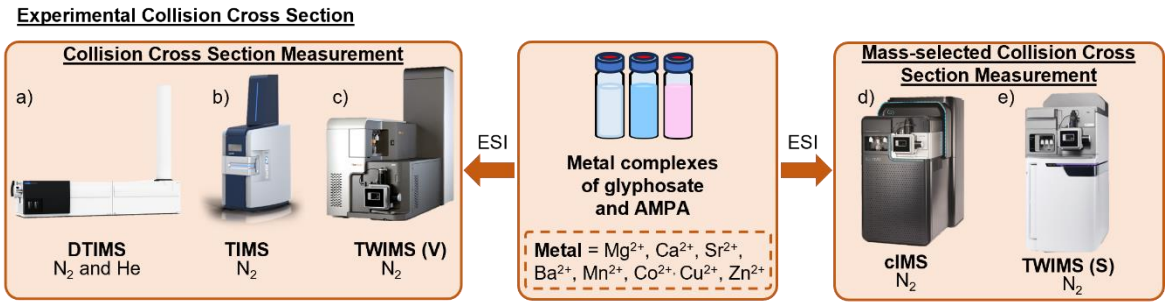

Scheme S1. Cross platform approach for obtaining the experimental CCS of glyphosate and AMPA metal complexes.

A cross-platform approach using 5 different IM-MS instruments (Scheme S1 a-e) and 6 experimental types (Scheme S1 a (N_2 and He) and b-e (N_2)) provides robust cross-platform conditions and enable generalization of structural categorization. Cross referencing with helium drift gas controls for any drift gas effects, important for metal complexes.[1,2]

Methanolic sample solutions containing either glyphosate or AMPA and each of the metal salts (as described) were prepared in desalted vials, resulting in 16 sample solutions. The pH of the solutions ranged from 4-5, with no pH adjustment carried out prior to analysis. The solutions were colourless, and all components were fully dissolved**.** This set of sample solutions were analysed via 5 different IM-MS instrument and 6 experiment types (Scheme S1). Different sets of methods were applied, depending on availability, including pre-mobility mass selection and automated CCS calibration (Table S1). The spectra produced by these methods were processed in their respective instrument software (see Experimental section for detail) and then analysed manually. From these resulting MS and IM spectra, qualitative inferences were drawn. Further, CCS_{exp} were derived for separated isoforms.

Table S1. Overview of the experiment types.

Instrument		IM	Mass Selection	CID	Peak Picking	Calibrant	Calibration Method
6560 IM LC/Q-ToF	a)	DTIMS (He)	No	No	Manual	Polyalanine	Calibration Curve
	a)	DTIMS (N_2)	No	No	Manual	Agilent TuneMix	Software automated
timsTOF Pro	b)	TIMS (N_2)	No	No	Manual	Agilent TuneMix	Software automated
Vion QToF	c)	TWIMS (N_2)	No	Yes	Auto + Manual	Polyalanine	Software automated
Select Series Cyclic IMS	d)	cIMS (N_2)	Yes	No	Manual	Agilent TuneMix	Calibration curve
Synapt XS	e)	TWIMS (N_2)	Yes	No	Manual	Polyalanine	Calibration curve

Ion Mobility Mass Spectrometry Methods

To ensure robustness across different ion mobility platforms, experiments were conducted on several ion mobility systems, namely, a Vion IMS QToF, Synapt XS, a SELECT Series cyclic IMS, a 6560 Ion Mobility Q-ToF and a tims-ToF Pro. Briefly, the Vion and Synapt instruments operate using traveling wave IM while the 6560 operates with drift tube IM and the tims-ToF Pro operates with trapped IM. Additionally, N_2 and He bath gas were used for measurements in the 6560. Specifics for each instrument are detailed below.

Vion IMS qToF (Waters Corporation)

Experimentally derived arrival time distributions and CCS values were obtained using a Vion IMS QTof (Waters Corporation) hybrid mass spectrometer system via direct infusion with a syringe pump using N_2 as the drift gas (TWIMS (Vion) $^{N2}CCS_{exp}$). The instrument was connected to an electrospray ionisation (ESI) source which was operated in positive polarity mode with the following parameters: capillary voltage: 3kV; source temperature: 120°C; cone voltage: 40 V; source offset: 80 V; collision energy: 15 eV; cone gas flow rate: 100L/h; desolvation temperature: 550°C; desolvation gas flow rate: 800 L/h; low collision energy: 6V and high collision energy: 45 V. The sample was infused at a rate of 10 uL/min. Data analysis and calculation of CCS was conducted using Waters UNIFI software using a lockspray reference mass of 556.2766 *m/z* infused at a flow rate of 10 µL/min. The spectra were acquired at a *m/z* range of 50-2000 for 1 minute using high definition MS^E ($HDMS^E$) mode. ^{N2}CCS values were automatically calculated by the software based on polyalanine calibration. Values corresponding to the *m/z* of interest were compiled without further processing.

Synapt XS (Waters Corporation)

The CCS measurements of glyphosate and AMPA metal complexes was performed on another TWIMS-MS platform, namely the Synapt XS. The main purpose of repeating the experiment on this platform is to perform pre-mobility mass-selection to filter out peaks that were being detected as a result of post-mobility dissociation. The sample was infused directly via a syringe pump connected to an ESI source at a flow rate of 10 µL/min. All spectra were acquired at a *m/z* range of 50-2000 for 1 minute. The instrument was mass and mobility calibrated on the day using Waters Major Mix IMS/ToF calibration kit. The instrument was operated in positive ion mode using N2 as the drift gas, with the following conditions: capillary voltage: 3kV; source temperature: 100 °C; cone voltage: 40 V; source offset: 30 V; cone gas flow rate: 50 L/h; desolvation temperature: 350 °C; desolvation gas flow rate: 600 L/h; IMS wave height: 40 V and IMS wave velocity: 183 m/s. Data analysis was then conducted using Waters DriftScope and MassLynx. CCS values for the mass-selected complexes of interest were the calculated based on a polyalanine calibration curve using methods previously outlined.[3]

SELECT SERIES Cyclic IMS (Waters Corporation)

The mass-selected experiment was repeated on the SELECT SERIES cyclic IMS (cIMS) platform for improved separation. The instrument was operated in positive ion mode and the sample was infused directly using a syringe pump connected to an ESI source at a flow rate of 10 µL/min. N_2 was used as the drift gas and the mass spectra were acquired at a *m/z* range of 50-2000 for 1 minute. The instrument was operated using the following conditions: capillary voltage: 2kV; source temperature: 100 °C, cone voltage: 40V; source offset: 10V; cone gas flow rate: 0 L/h; desolvation temperature: 250 °C; desolvation gas flow rate: 800 L/h; IMS wave height: 22 V and IMS wave velocity: 375 m/s. Data was acquired after 1 and 2 cycles around the mobility cell amounting to a total time of 22 and 44 ms, respectively. The additional cycle didn't yield further separation, so data from 1 cycle was used. CCS calibration was conducted using Agilent tuning mix following the equation reported in the study by Hennrich *et al.*[4]

6560 Ion Mobility qToF (Agilent Technologies)

Experimentally derived arrival time distributions and CCS values were also obtained with an Agilent 6560 IM-LC-QTOF system equipped with an electrospray ionisation (ESI) source. The drift gases N_2 and He were used and corresponding CCS values were obtained accordingly (DTIMS $^{N2}CCS_{exp}$, DTIMS $^{He}CCS_{exp}$). The instrument was calibrated on the day of the experiment using the Agilent tuning mix to ensure accuracy and minimise variability. The working principles of the drift tube can be derived directly from the low field equation.[5] The instrument was operated in positive mode using the following conditions: N_2 drying gas temperature of 300 °C and flow of 8 L/min; nebulizing gas pressure of 30 psi; sheath gas temperature and flow rate of 300 °C and 12 L/min, respectively. The data was collected with a frame rate of 1 and a *m/z* scan range of 100-3200. The drift tube was operated with the following parameters: N2 collision gas; trap fill time of 5000 µs; trap release time of 150 µs; IM transient rate of 16;

drift tube entrance voltage of 1700 V; drift tube exit voltage of 250 V; drift tube temperature of 33 °C and drift tube pressure of 3.94 Torr.

The data obtained were viewed and processed using the MassHunter IM-MS Browser ver. B.07.01 software. The β (m) and t-fix values were automatically calculated from the software based on the tuning mix data file obtained on the day, which can then be used to apply the appropriate correction to all data files obtained on the same day. CCS were then calculated using their experimental drift time as derived from first principle based on the low field equation . For He CCS values, CCS were conducted manually by using polyalanine as the calibrant. Based on literature CCS values for polyalanine,[6] we conducted a curve fitting where we plotted the recorded drift time for the alanine peaks against the CCS/μ value where μ = reduced mass. The resulting equation were then used to calculate CCS of Glyphosate-M and AMPA-M complexes of interest in He.

tims-ToF Pro (Bruker Daltonics)

A tandem trapped ion mobility spectrometry (TIMS) – ToF Pro from Bruker was used to obtain CCS values of Glyphosate and AMPA metal complexes. Prior to data acquisition, the instrument was calibrated using Agilent TuneMix solution. Samples were directly infused into the ESI source at a flow rate of 10 μL/min and N_2 was used as the drift gas. The ionisation conditions used were as follows: capillary voltage: 4kV; drying gas flow rate: 3.5 L/min; drying gas temperature: 200 °C; $1/K_0$ range: 0.2-2 Vs cm^{-2}; ramp time: 1160 ms. Data obtained on the TIMS were viewed and processed using Compass Data Analysis software. Values measured on TIMS are derived as $1/K_0$. Charge assignments were completed manually, and CCS were automatically calculated by the software based on Agilent ESI-L low concentration tuning mix calibration.

IM-IRMPD-MS

The samples were then analysed using ESI-IM-IRMPD-MS on a modified Synapt G2, namely, the Photo-Synapt.[7] The modification enabled ion mobility slicing and, after ion mobility, trapping of the ions in hexapole pin traps. This, together with optical access for laser systems, allows for infrared spectroscopic investigations of mass- and mobility selected ions. The experiments were conducted using an MSquared FireFly infrared laser. In short, the intensity of precursor and fragment ions was recorded as a function of the wavelength, after which they were converted to IRMPD yield via $-\ln\left(\frac{I_{precursor}}{\sum I_{fragments}+I_{precursor}}\right)$.

$[Ba+glyphosate-H]^+$ ions were mass- and mobility selected, after which they were trapped and irradiated by the IR laser for 1500 ms. The graph in Figure 6 in the main text is an averaged spectrum of several scans: 2 times a scan between 2700 and 3700 cm^{-1} with a 2 cm^{-1} step size, and 4 times a finer scan between 3500-3700 cm^{-1} with a 1 cm^{-1} step size. The samples were directly infused into the ESI source using a syringe pump at a flow rate of 3 μL/min with N2 as the drift gas. The instrument was operated in positive mode with the following settings: capillary voltage: 2.1kV; source temperature: 80 °C; cone voltage: 50 V; cone gas flow rate: 0 L/h; desolvation temperature: 150 °C; desolvation gas flow rate: 500 L/h; IMS wave height: 20 V and IMS wave velocity: 490 m/s.

LTQ-Orbitrap-XL Mass Spectra

Typical mass spectra when analysing glyphosate-M and AMPA-M complexes using ESI-MS highlighting various complexes formed. Identification of key peaks are listed on the relevant Tables.

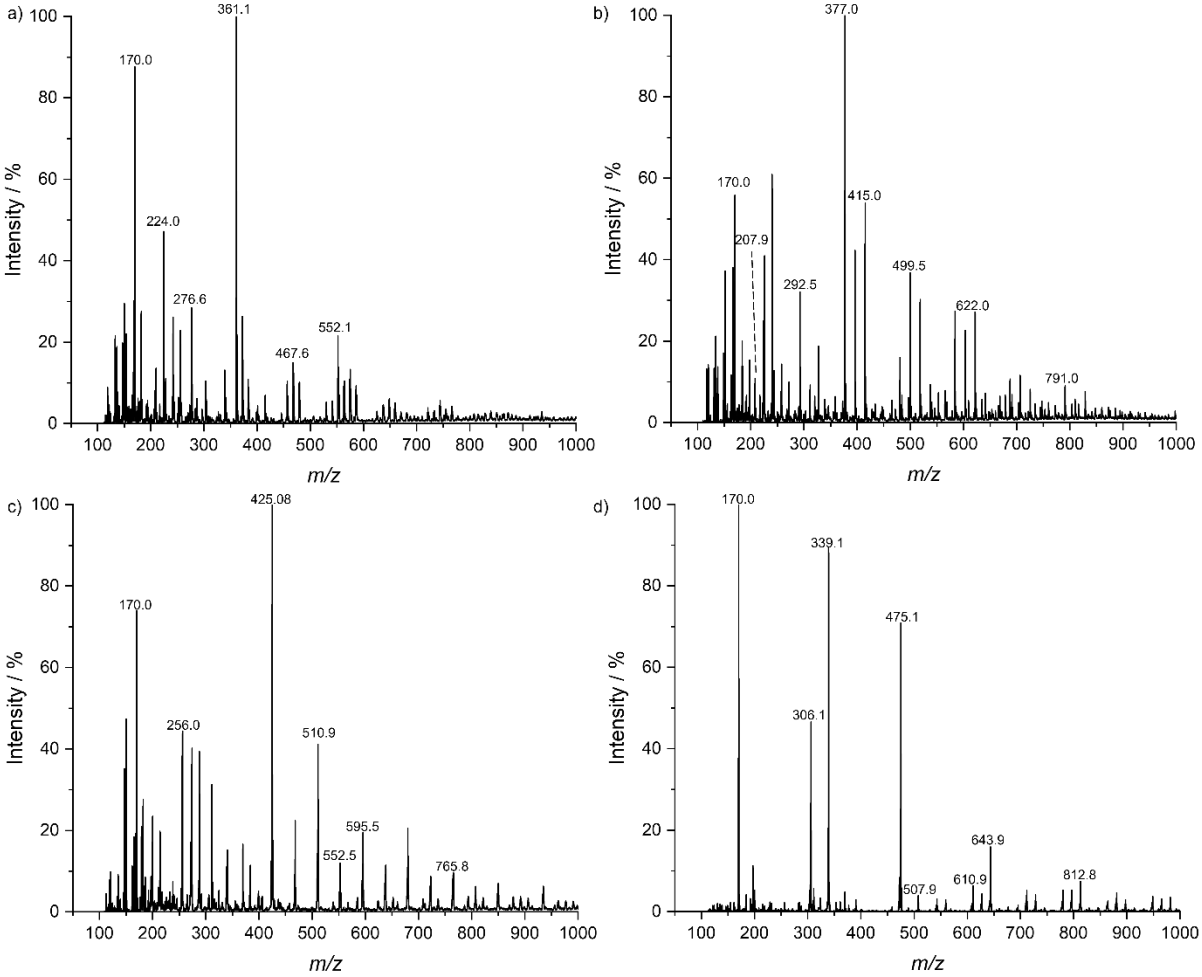

Figure S1. Mass spectra of $[M+glyphosate-H]^+$ where M is a) Mg^{2+}, b) Ca^{2+}, c) Sr^{2+}, and d) Ba^{2+} obtained on the Orbitrap. Assigned *m/z* values are listed on Table S2.

Table S2. Mass assignment for Figure S1

Sample	*m/z*	Assignment
Glyphosate-Mg	170	$[glyphosate+H]^+$
	224	$[Na+Glyphosate-H+MeOH]^+$
	276.6	$[2Mg+3glyphosate-2H]^+$
	361.1	$[Mg+2glyphosate-H]^+$
	467.6	$[4Mg+5glyphosate-6H]^{2+}$
	552.1*	$[2Mg+3glyphosate-3H]^+$
Glyphosate-Ca	170	$[glyphosate+H]^+$
	207.9	$[Ca+glyphosate-H]^+$
	292.5	$[2Ca+3glyphosate-2H]^{2+}$
	377	$[Ca+2glyphosate-H]^+$
	415	$[2Ca+2glyphosate-3H]^+$
	499.5	$[4Ca+5glyphosate-6H]^{2+}$
	622*	$[3Ca+3glyphosate-5H]^+$
	791*	$[3Ca+4glyphosate-5H]^+$
Glyphosate-Sr	170	$[glyphosate+H]^+$
	256	$[Sr+glyphosate-H]^+$
	425.1	$[Sr+2glyphosate-H]^+$
	510.9	$[2Sr+2glyphosate-3H]^+$
	552.5	$[3Sr+5glyphosate-4H]^{2+}$
	595.5	$[4Sr+5glyphosate-6H]^{2+}$
	765.8*	$[3Sr+3glyphosate-5H]^+$
Glyphosate-Ba	170	$[glyphosate+H]^+$
	306.1	$[Ba+glyphosate-H]^+$
	339.1	$[2glyphosate=H]^+$
	475.1	$[Ba+2glyphosate-H]^+$
	507.9	$[3glyphosate+H]^+$
	610.9	$[2Ba+2glyphosate-3H]^+$
	643.9	$[Ba+3glyphosate-H]^+$
	812.8	$[Ba+4glyphosate-H]^+$

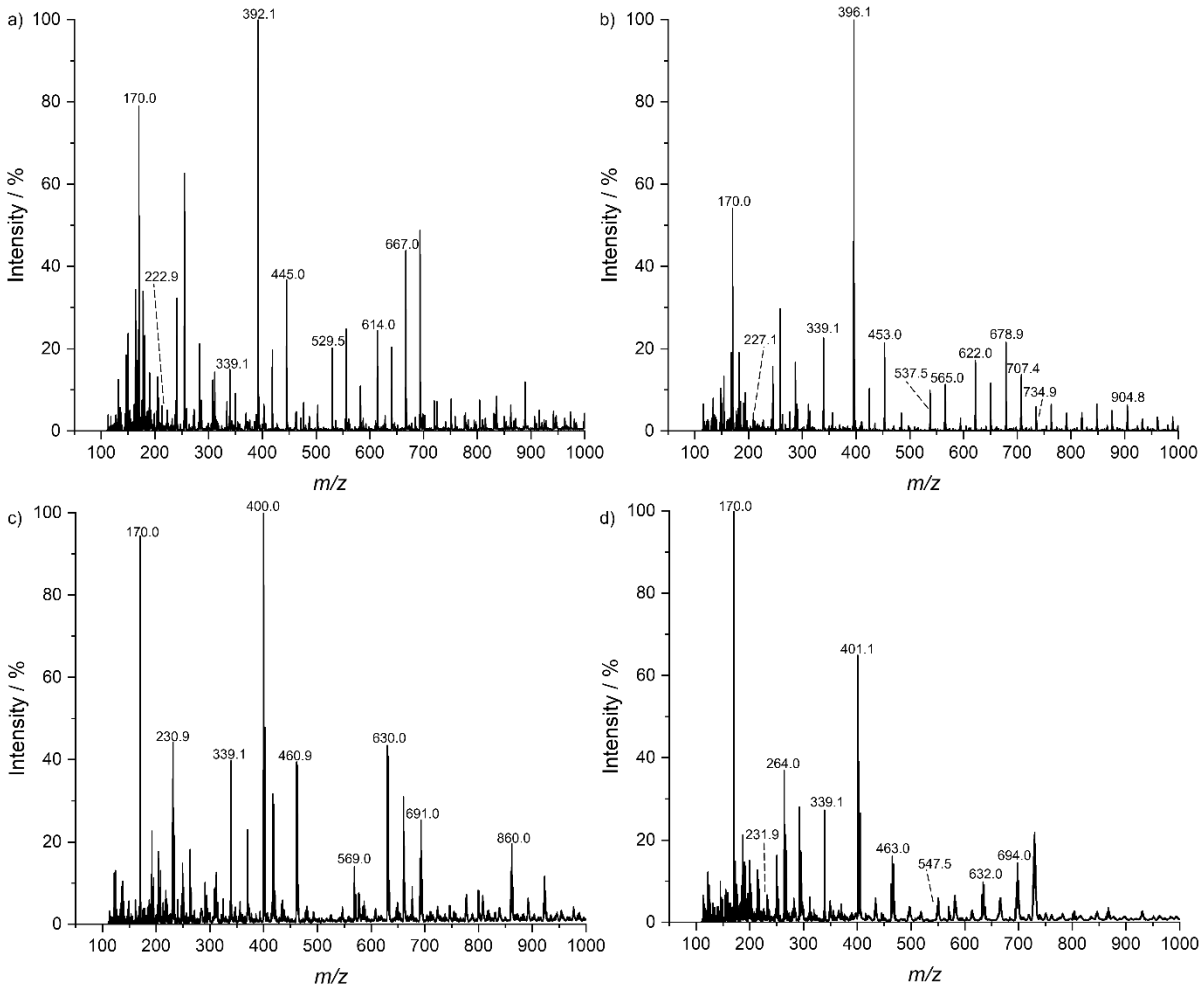

Figure S2. Mass spectra of $[M+glyphosate-H]^+$ where M is a) Mn^{2+}, b) Co^{2+}, c) Cu^{2+}, and d) Zn^{2+} obtained on the Orbitrap. Assigned *m/z* values are listed on Table S3.

Table S3. Assignment for Figure S2

Sample	*m/z*	Assignment
Glyphosate-Mn	170	$[glyphosate+H]^+$
	222.9	$[Mn+glyphosate-H]^+$
	339.1	$[2glyphosate+H]^+$
	392.1	$[Mn+2glyphosate-H]^+$
	445	$[2Mn+2glyphosate-3H]^+$
	529.5	$[4Mn+5glyphosate-6H]^{2+}$
	614*	$[2Mn+3glyphosate-3H]^+$
	667*	$[3Mn+3glyphosate-5H]^+$
Glyphosate-Co	170	$[glyphosate+H]^+$
	227.1	$[Co+glyphosate-H]^+$
	339.1	$[2glyphosate-H]^+$
	396.1	$[Co+2glyphosate-H]^+$
	453	$[2Co+2glyphosate-3H]^+$
	537.5	$[4Co+5glyphosate-6H]^{2+}$
	565	$[Co+3glyphosate]^+$
	622	$[2Co+3glyphosate-3H]^+$
	678.9*	$[3Co+3glyphosate-5H]^+$
	707.4	$[4Co+7glyphosate-6H]^{2+}$
	734.9	$[Co+4glyphosate-H]^+$
	904.8	$[Co+5glyphosate-H]^+$
Glyphosate-Cu	170	$[glyphosate+H]^+$
	230.9	$[Cu+glyphosate-H]^+$
	339.1	$[2glyphosate+H]^+$
	400	$[Cu+2glyphosate-H]^+$
	460.9	$[2Cu+2glyphosate-3H]^+$
	569	$[Cu+3glyphosate]^+$
	630	$[2Cu+3glyphosate-3H]^+$
	691*	$[3Cu+3glyphosate-5H]^+$
	860*	$[3Cu+4glyphosate-5H]^+$
Glyphosate-Zn	170	$[glyphosate+H]^+$
	231.9	$[Zn+glyphosate-H]^+$
	264	$[Zn+glyphosate-H+MeOH]^+$
	339.1	$[2glyphosate+H]^+$
	401.1	$[Zn+2glyphosate-H]^+$
	463	$[2Zn+2glyphosate-3H]^+$
	547.5	$[4Zn+5glyphosate-6H]^{2+}$
	632*	$[2Zn+3glyphosate-3H]^+$
	694*	$[3Zn+3glyphosate-5H]^+$

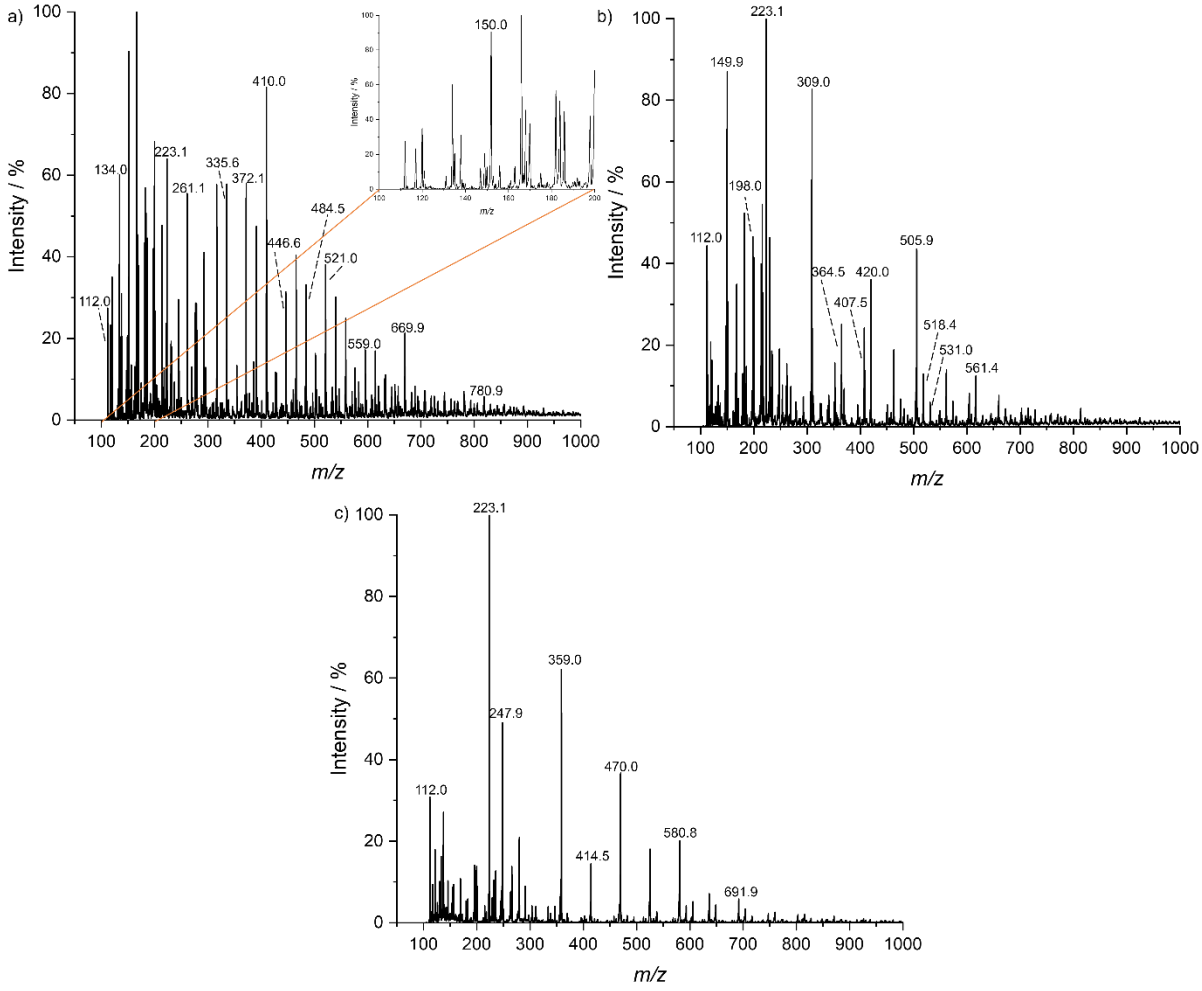

Figure S3. Mass spectra of $[M+AMPA-H]^+$ where M is a) Ca^{2+}, b) Sr^{2+}, and c) Ba^{2+} obtained on the Orbitrap. Assigned *m/z* values are listed on Table S4.

Table S4. Mass assignment for Figure S3

Sample	*m/z*	Assignment
AMPA-Ca	112	$[AMPA+H]^+$
	134	$[AMPA+Na]^+$
	223.1	$[2AMPA+H]^+$
	261.1	$[Ca+2AMPA-H]^+$
	335.6	$[3Ca+5AMPA-4H]^{2+}$
	372.1	$[Ca+3AMPA-H]^+$
	410	$[2Ca+3AMPA-3H]^+$
	446.5	$[3Ca+7AMPA-4H]^{2+}$
	484.5	$[2Ca+4AMPA-3H]^+$
	521	$[Ca+3AMPA-H]^+$
	559	$[5Ca+9AMPA-8H]^{2+}$
	669.9*	$[3Ca+5AMPA-5H]^+$
	780.9*	$[3Ca+6AMPA-5H]^+$
AMPA-Sr	112	$[AMPA+H]^+$
	149.9	$[AMPA+K]^+$
	198	$[Sr+AMPA-H]^+$
	223.1	$[2AMPA+H]^+$
	309	$[Sr+2AMPA-H]^+$
	364.5	$2Sr+5AMPA-2H]^{2+}$
	407.5	$[3Sr+5AMPA-4H]^{2+}$
	420	$[Sr+3AMPA-H]^+$
	505.9	$[2Sr+3AMPA-3H]^+$
	518.4	$[3Sr+7AMPA-4H]^{2+}$
	531*	$[Sr+4AMPA-H]^+$
	561.4*	$[4Sr+7AMPA-6H]^+$
AMPA-Ba	112	$[AMPA+H]^+$
	223.1	$[2AMPA+H]^+$
	247.9	$[Ba+AMPA-H]^+$
	359	$[Ba+2AMPA-H]^+$
	414.5	$[2Ba+5AMPA-2H]^+$
	470	$[Ba+3AMPA-H]^+$
	580.8	$[Ba+4AMPA-H]^+$
	691.9	$[Ba+5AMPA-H]^+$

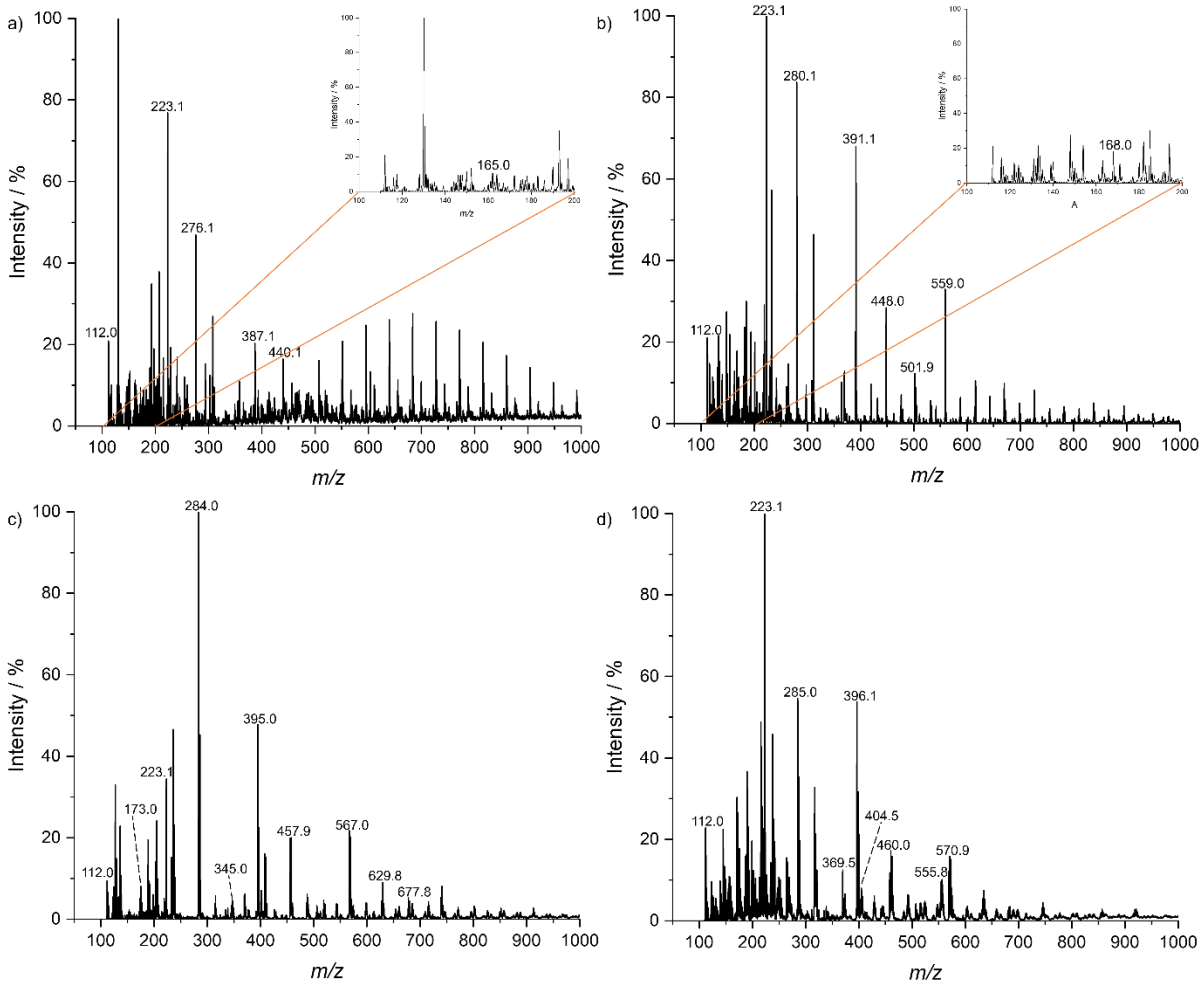

Figure S4. Mass spectra of $[M+AMPA-H]^+$ where M is a) Mn^{2+}, b) Co^{2+}, c) Cu^{2+}, and d) Zn^{2+} obtained on the Orbitrap. Assigned *m/z* values are listed on Table S5.

Table S5. Mass assignment for Figure S4

Sample	*m/z*	Assignment
AMPA-Mn	112	$[AMPA+H]^+$
	223.1	$[2AMPA+H]^+$
	276.1	$[Mn+2AMPA-H]^+$
	387.1	$[Mn+3AMPA-H]^+$
	440.1	$[2Mn+3AMPA-H]^+$
AMPA-Co	112.1	$[AMPA+H]^+$
	223.1	$[2AMPA+H]^+$
	280.1	$[Co+2AMPA-H]^+$
	391.1	$[Co+3AMPA-H]^+$
	448	$[2Co+3AMPA-3H]^+$
	501.9	$[Co+4AMPA-H]^+$
	559	$[2Co+4AMPA-3H]^+$
AMPA-Cu	112	$[AMPA+H]^+$
	173	$[Cu+AMPA-H]^+$
	223.1	$[2AMPA+H]^+$
	284	$[Cu+2AMPA-H]^+$
	345	$[2Cu+2AMPA-3H]^+$
	395	$[Cu+3AMPA-H]^+$
	456	$[2Cu+3AMPA-3H]^+$
	567*	$[2Cu+4AMPA-3H]^+$
	628*	$[3Cu+4AMPA-5H]^+$
	678	$[2Cu+5AMPA-3H]^+$
AMPA-Zn	112	$[AMPA+H]^+$
	223.1	$[2AMPA+H]^+$
	285	$[Zn+2AMPA-H]^+$
	369.5	$[3Zn+5AMPA-4H]^{2+}$
	396.1	$[3Zn+5AMPA-H]^+$
	404.5	$[4Zn+5AMPA-6H]^{2+}$
	460	$[2Zn+3AMPA-3H]^+$
	555.8	$[5AMPA+H]^+$
	570.9	$[2Zn+4AMPA-3H]^+$

IM-MS (TWIMS (Vion)) heat map showing isomeric assemblies

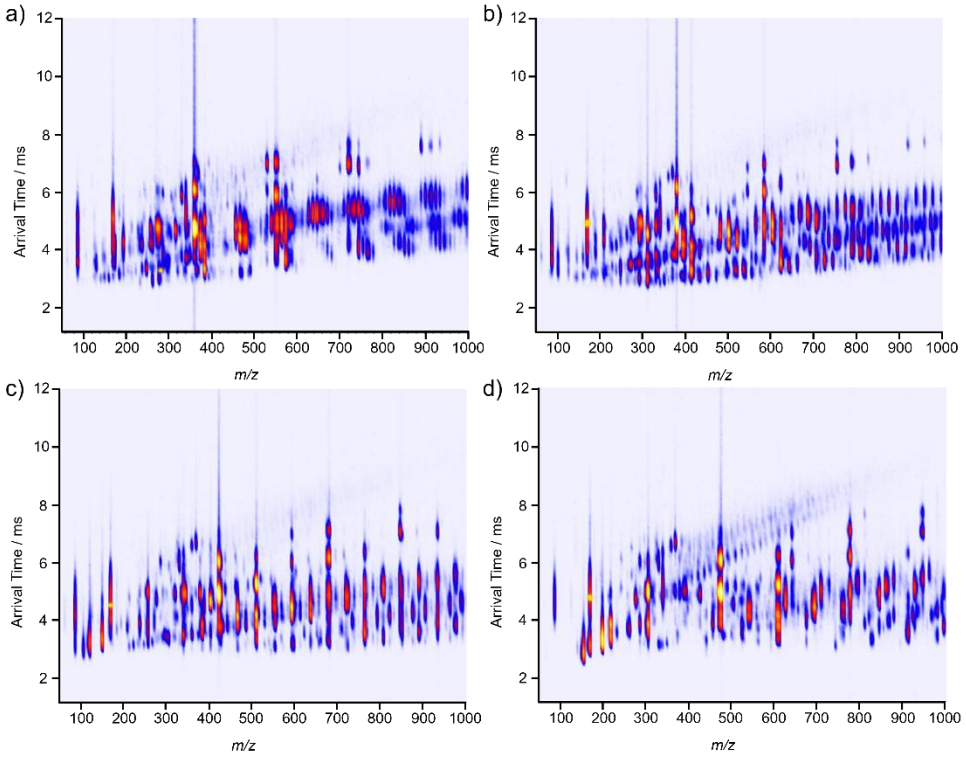

Figure S5. IM-MS heatmap of [M+glyphosate−H]$^{+}$ where M is a) Mg^{2+}, b) Ca^{2+}, c) Sr^{2+}, and d) Ba^{2+}

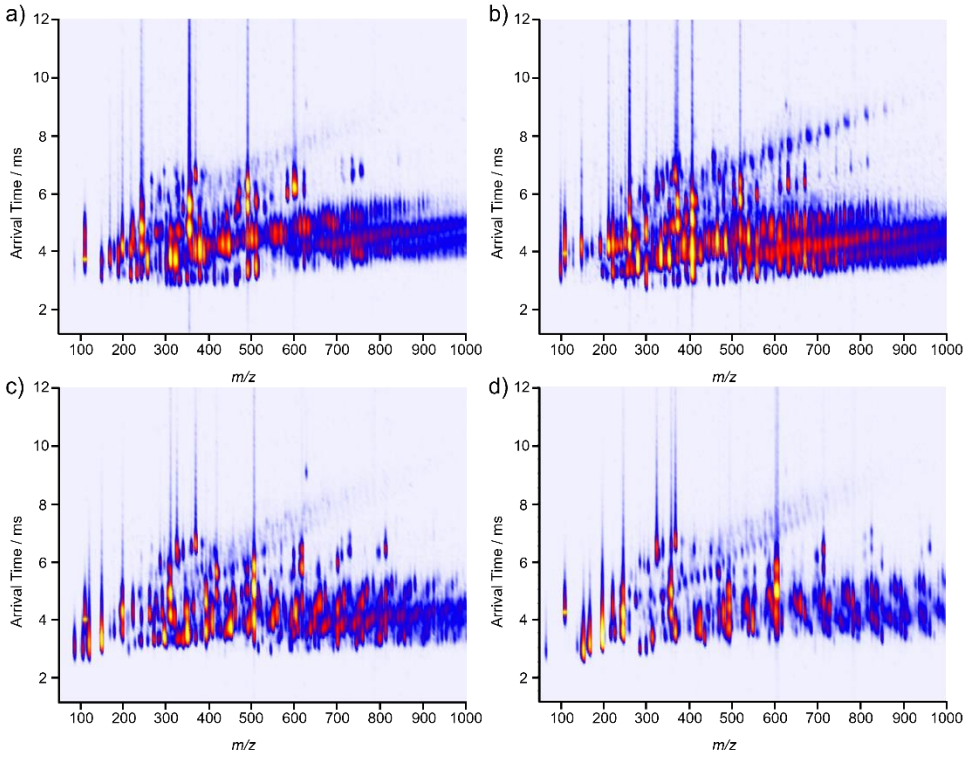

Figure S6. IM-MS heatmap of [M+glyphosate−H]$^{+}$ where M is a) Mn^{2+}, b) Co^{2+}, c) Cu^{2+}, and d) Zn^{2+}

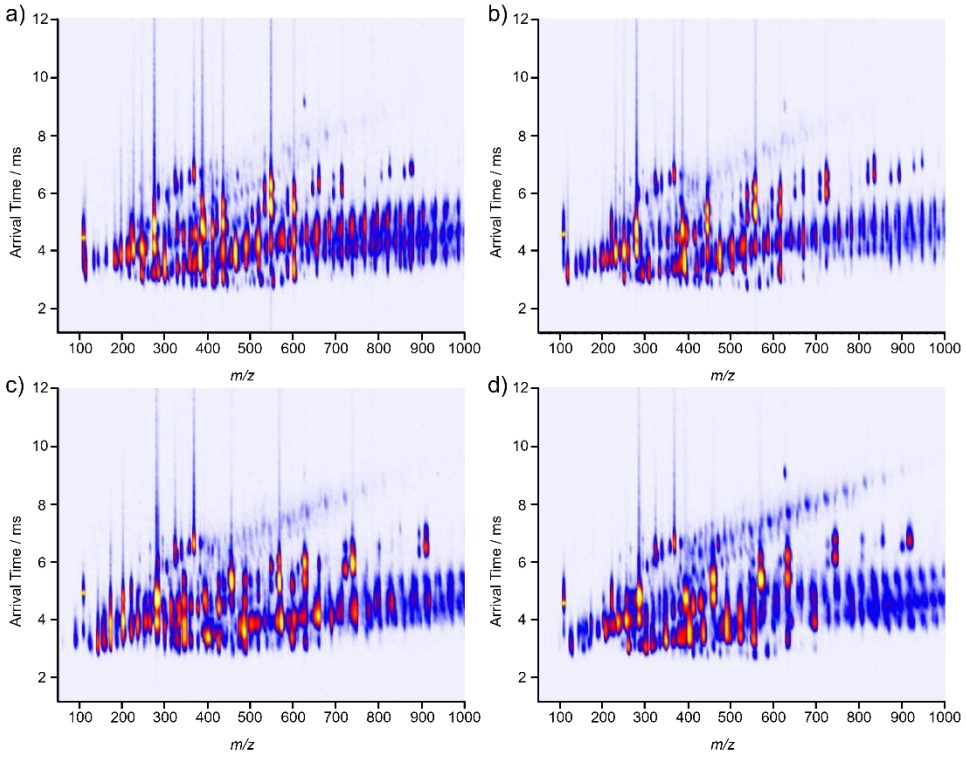

Figure S7. IM-MS heatmap of $[M+AMPA-H]^+$ where M is a) Mg^{2+}, b) Ca^{2+}, c) Sr^{2+}, and d) Ba^{2+}

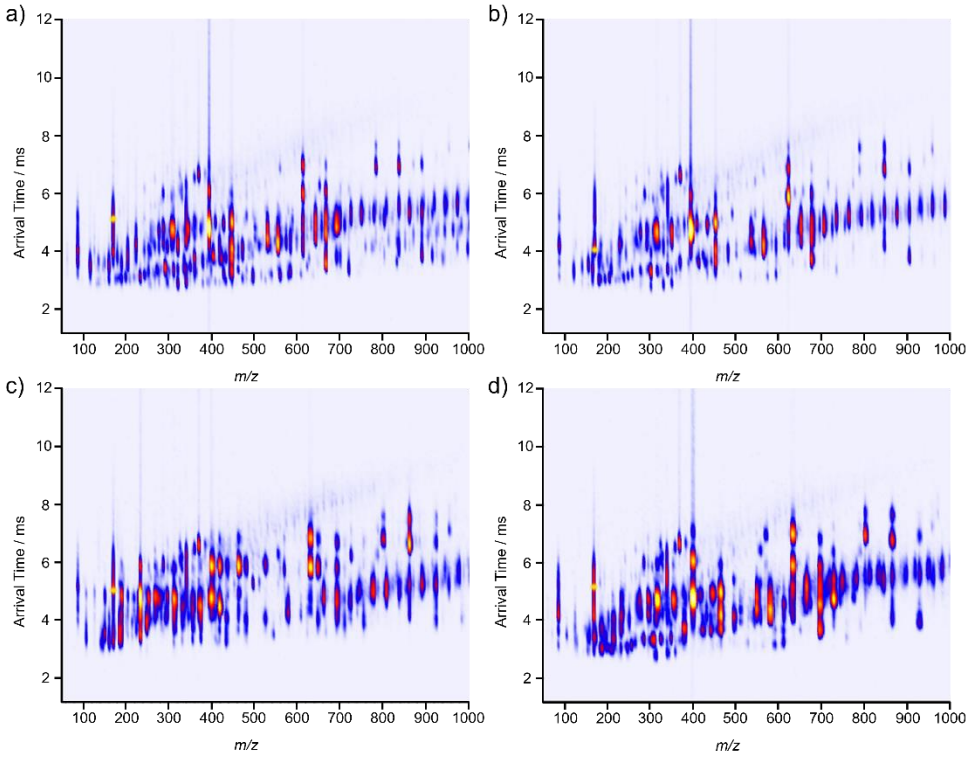

Figure S8. IM-MS heatmap of $[M+AMPA-H]^+$ where M is a) Mn^{2+}, b) Co^{2+}, c) Cu^{2+}, and d) Zn^{2+}

Arrival time distribution of [M+glyphosate−H]$^+$ and [M+AMPA−H]$^+$ on non-mass-selected TWIMS (Vion)

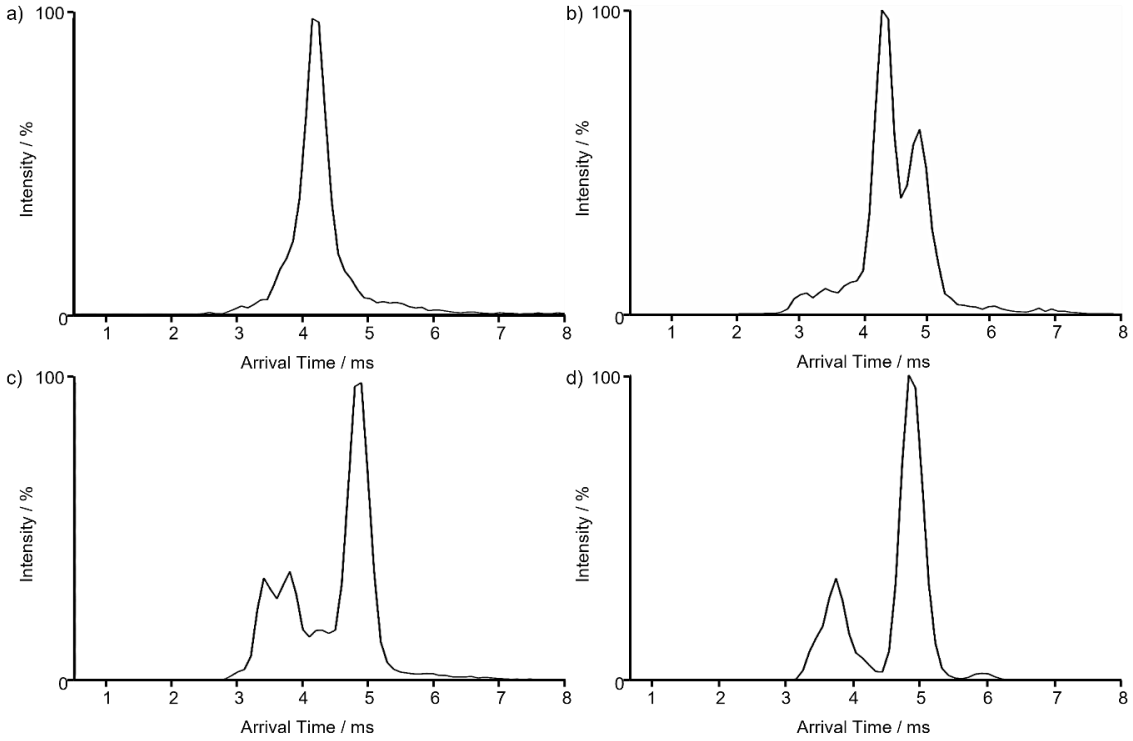

Figure S9. Arrival time distribution for [M+glyphosate−H]$^+$ where M is a) Mg^{2+}, b) Ca^{2+}, c) Sr^{2+}, and d) Ba^{2+} on the Vion

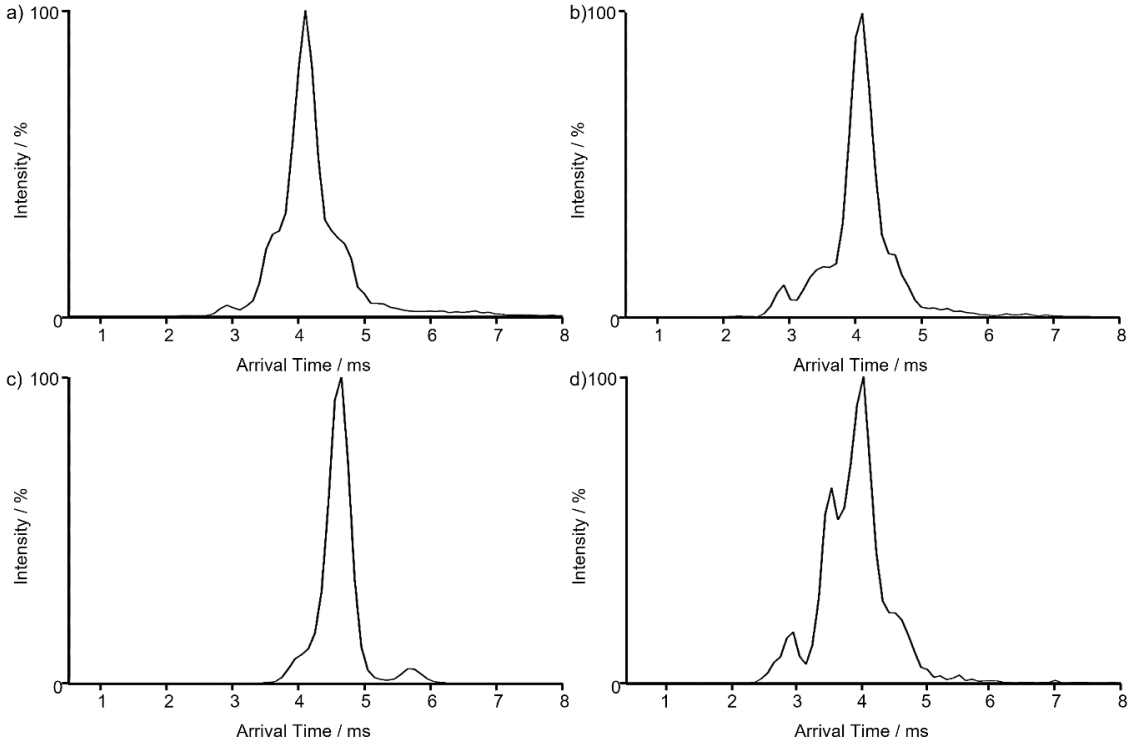

Figure S10. Arrival time distribution for [M+glyphosate−H]$^+$ where M is a) Mn^{2+}, b) Co^{2+}, c) Cu^{2+}, and d) Zn^{2+} on the Vion

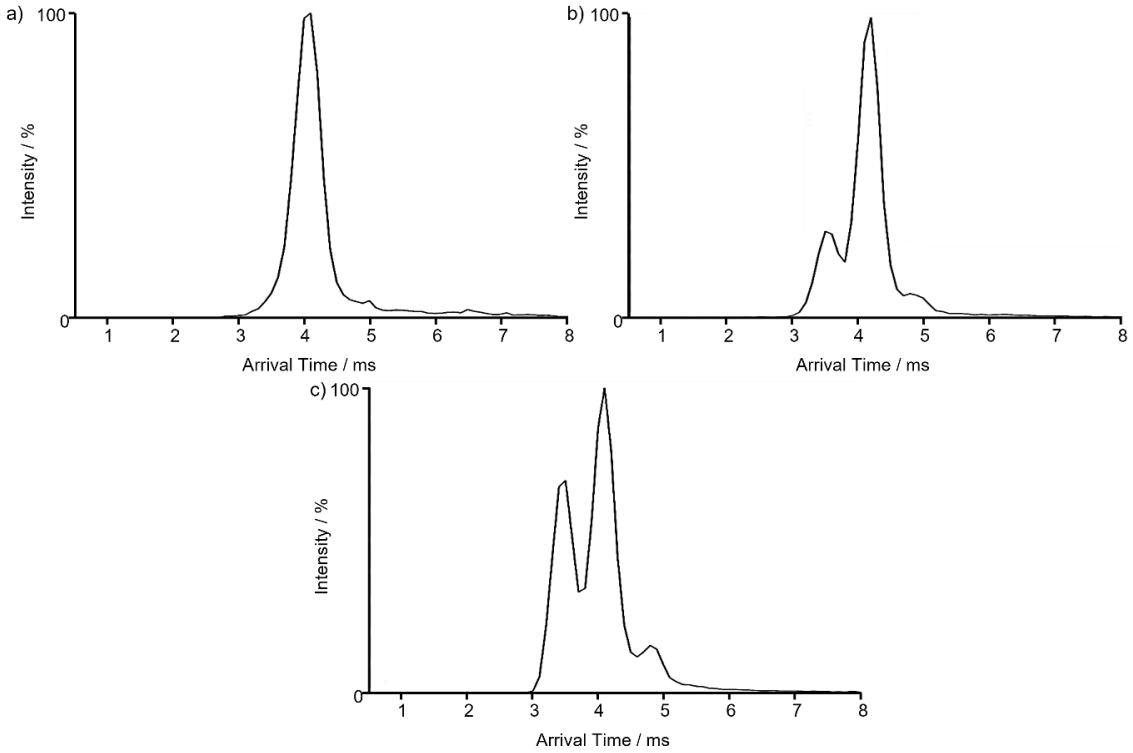

Figure S11. Arrival time distribution for $[M+AMPA-H]^+$ where M is a) Ca^{2+}, b) Sr^{2+}, and c) Ba^{2+} on the Vion

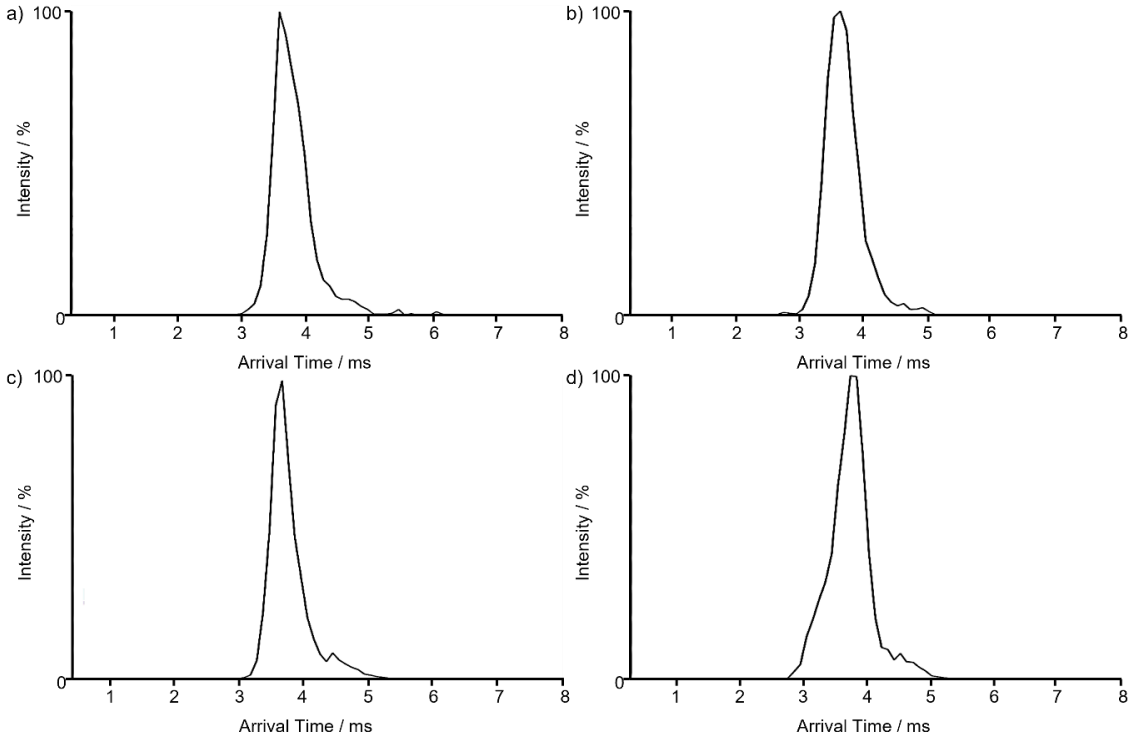

Figure S12. Arrival time distribution for $[M+AMPA-H]^+$ where M is a) Mn^{2+}, b) Co^{2+}, c) Cu^{2+}, and d) Zn^{2+} on the Vion

Arrival time distribution of [M+glyphosate−H]$^{+}$ and [M+AMPA−H]$^{+}$ on mass-selected TWIMS (Synapt)

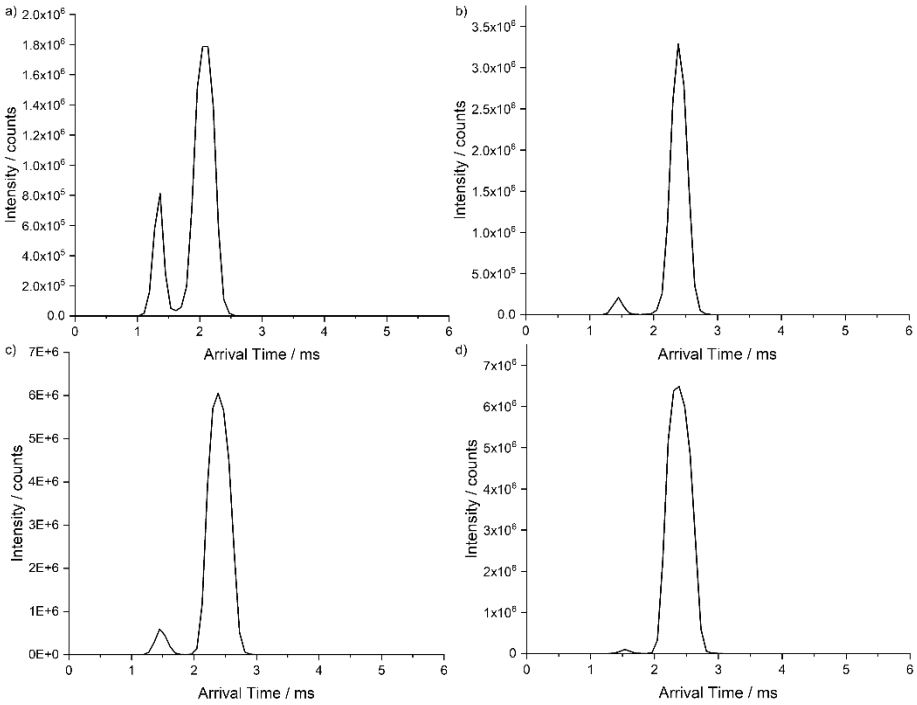

Figure S13. Arrival time distribution for mass-selected [M+glyphosate−H]$^{+}$ where M is a) Mg^{2+}, b) Ca^{2+}, c) Sr^{2+}, and d) Ba^{2+} on the Synapt

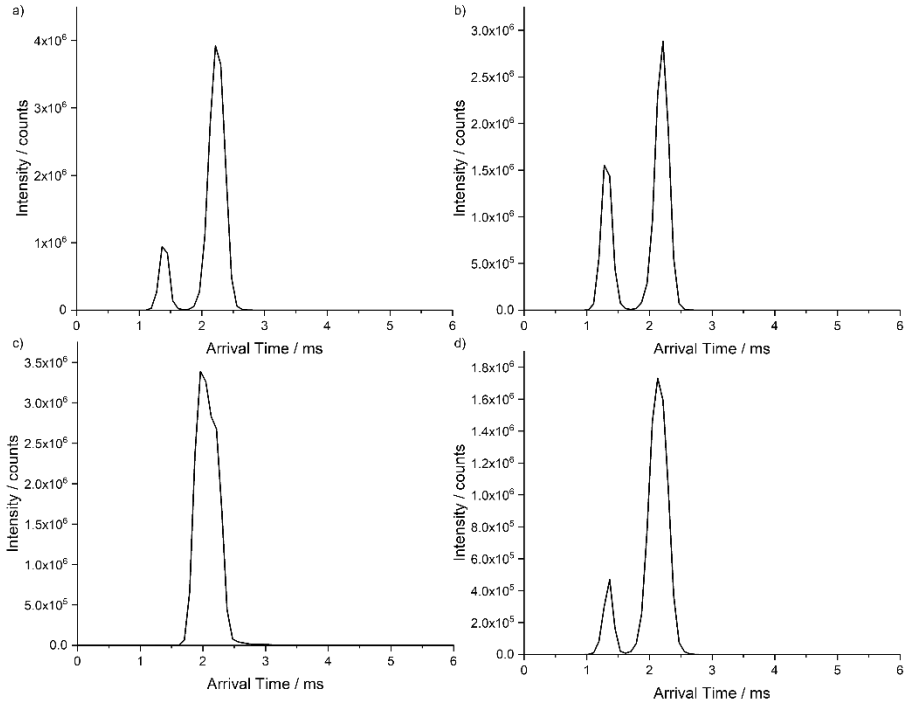

Figure S14. Arrival time distribution for mass-selected [M+glyphosate−H]$^{+}$ where M is a) Mn^{2+}, b) Co^{2+}, c) Cu^{2+}, and d) Zn^{2+} on the Synapt

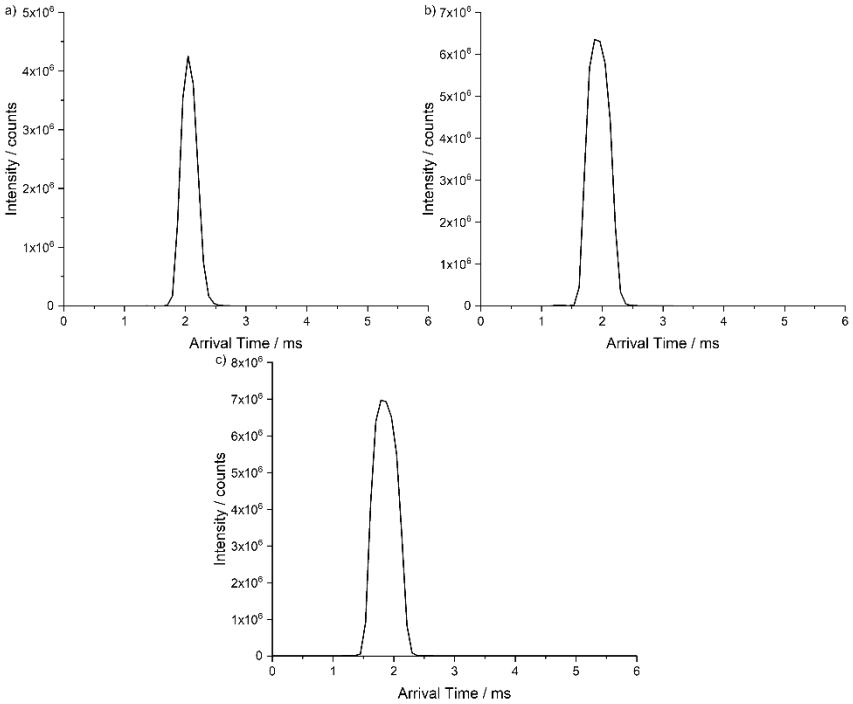

Figure S15. Arrival time distribution for mass-selected $[M+AMPA-H]^+$ where M is a) Ca^{2+}, b) Sr^{2+}, and c) Ba^{2+} on the Synapt

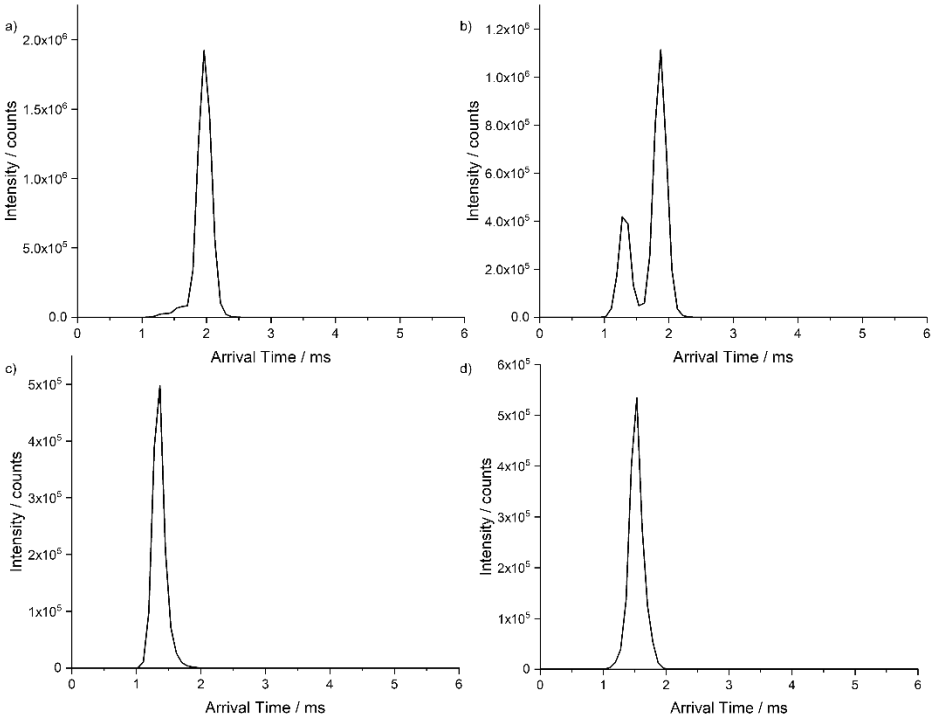

Figure S16. Arrival time distribution for mass-selected $[M+AMPA-H]^+$ where M is a) Mn^{2+}, b) Co^{2+}, c) Cu^{2+}, and d) Zn^{2+} on the Synapt

Arrival time distribution of mass-selected [M+glyphosate−H]$^+$ and [M+AMPA−H]$^+$ on cIMS

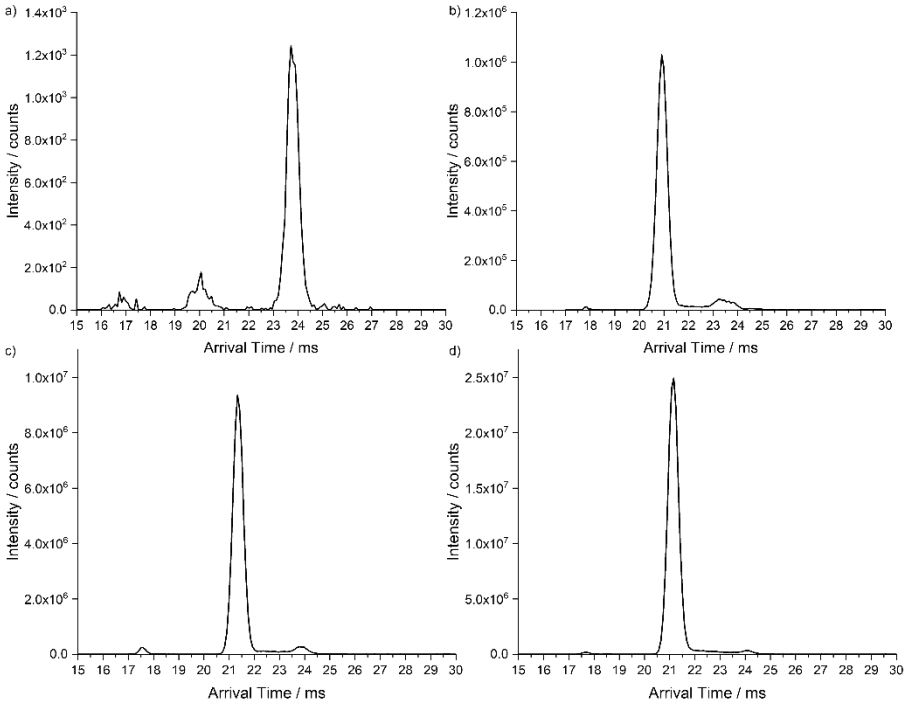

Figure S17. Arrival time distribution for mass-selected [M+glyphosate−H]$^+$ where M is a) Mg^{2+}, b) Ca^{2+}, c) Sr^{2+}, and d) Ba^{2+} on the cIMS

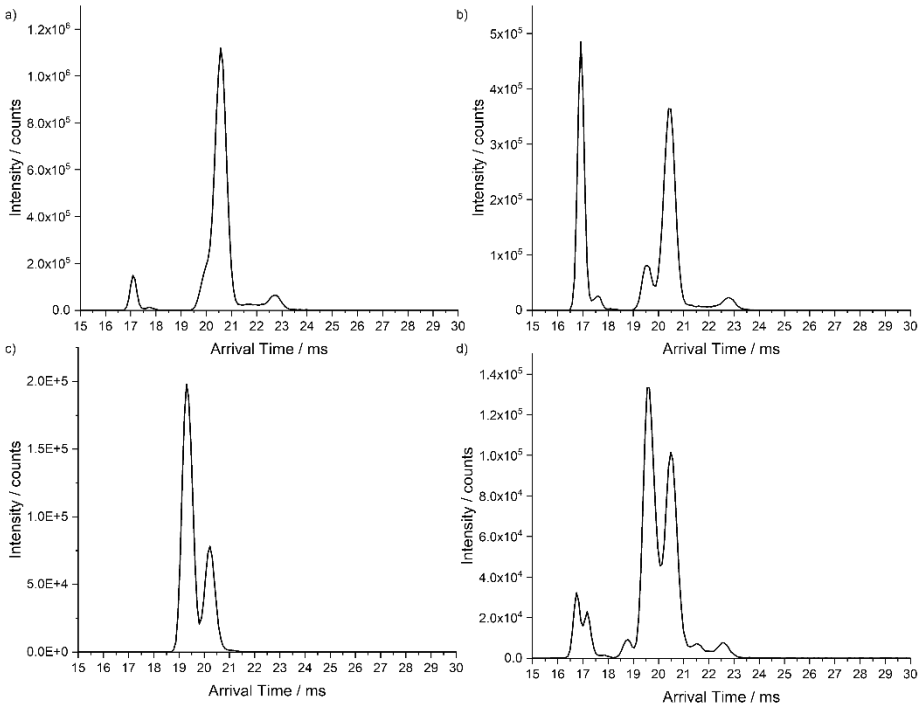

Figure S18. Arrival time distribution for mass-selected [M+glyphosate−H]$^+$ where M is a) Mn^{2+}, b) Co^{2+}, c) Cu^{2+}, and d) Zn^{2+} on the cIMS

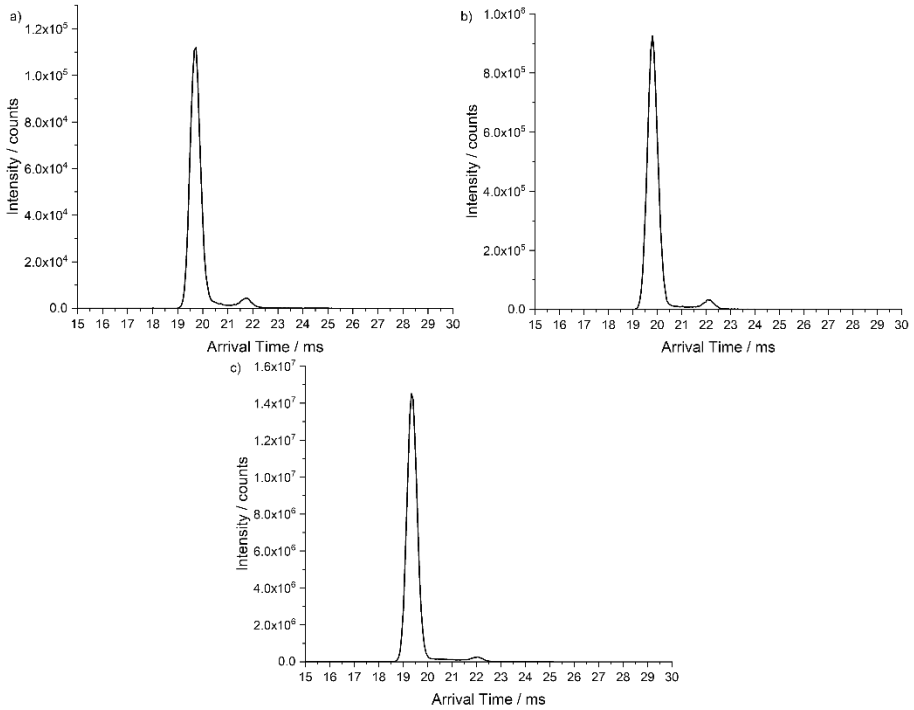

Figure S19. Arrival time distribution for mass-selected $[M+AMPA-H]^+$ where M is a) Ca^{2+}, b) Sr^{2+}, and c) Ba^{2+} on the cIMS

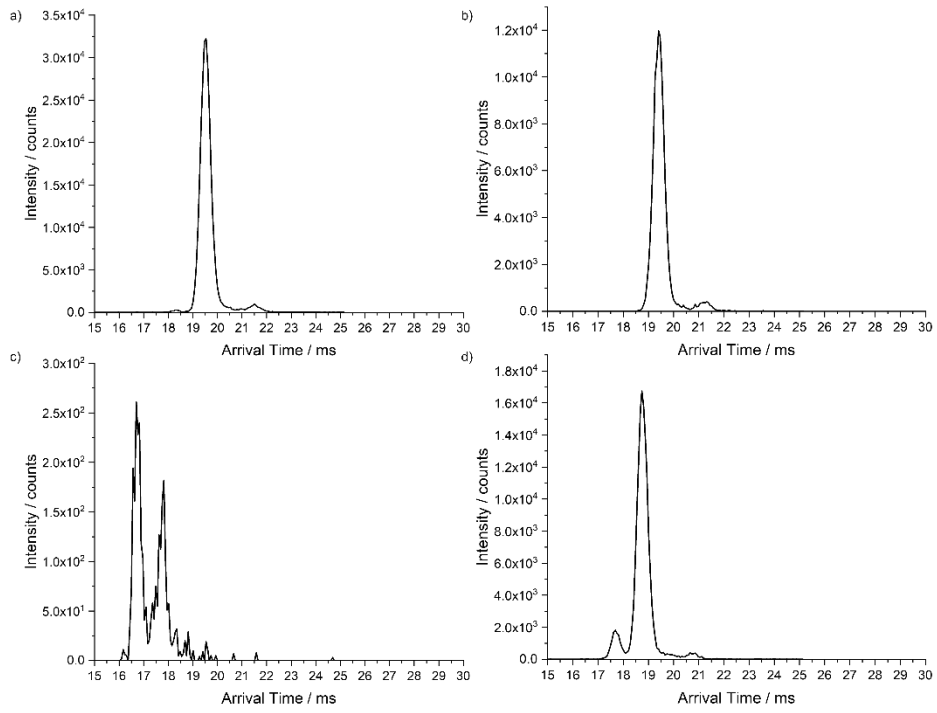

Figure S20. Arrival time distribution for mass-selected $[M+AMPA-H]^+$ where M is a) Ca^{2+}, b) Sr^{2+}, and c) Ba^{2+} on the cIMS

Table S6. Apparent number of (a) peaks observed by IM separation and (b) their collisional cross sections, (CCS_{exp}, Å^2) for [M+glyphosate−H]$^+$ where M=Mg^{2+}, Ca^{2+}, Sr^{2+}, and Ba^{2+}.

M	**Mg^{2+}**		**Ca^{2+}**		**Sr^{2+}**		**Ba^{2+}**	
	(a)	(b) Å^2	(a)	(b) Å^2	(a)	(b) Å^2	(a)	(b) Å^2
DTIMS (N2)	2	146.5 172	4	125 132 146.5 157.5	1	147.7	2	139.4 148
TIMS(N2)	2	138.2 144.4	4	124.1 138.6 176.9 214.6	4	124.9 139.6 177.3 212.5	5	126.5 131.4 138.9 177.3 191.8
TWIMS (V) (N2)	2	153.4 185.4	5	158.4 173.8 123.9 208.3 234.1	3	172.8 139.2 204.7	3	173.7 140.9 204.1
DTIMS (He)	2	62.3 114.0	2	65.4 71.9	3	68.5 83.6 104.0	3	58.4 68.4 99.1

Table S7. Apparent number of (a) peaks observed by IM separation and (b) their collisional cross sections, (CCS_{exp}, Å^2) for [M+glyphosate−H]$^+$ where M=Mn^{2+}, Co^{2+}, Cu^{2+}, and Zn^{2+}.

M	**Mn^{2+}**		**Co^{2+}**		**Cu^{2+}**		**Zn^{2+}**	
	(a)	(b) Å^2	(a)	(b) Å^2	(a)	(b) Å^2	(a)	(b) Å^2
DTIMS (N2)	2	147.3 160.2	2	145.7 152.9	1	171.5	3	136.9 141.4 144.2
TIMS(N2)	2	126 151.3	3	127.4 135.4 157.5	3	152.9 163.3 172.6	2	126.6 155.9 159.6
TWIMS (V) (N2)	2	154.3 122.1	2	152.6 125.3	3	168.7 199.1 232.6	1	149.2
DTIMS (He)	3	65.4 70.6 82.4	3	63.6 70.0 75.0	4	62.0 72.7 90.4 104.7	5	55.0 62.7 70.2 76.2 81.6

Table S8. Apparent number of (a) peaks observed by IM separation and (b) their collisional cross sections, (CCS_{exp}, Å^2) for $[M+AMPA-H]^+$ where M= Ca^{2+}, Sr^{2+}, and Ba^{2+}.

M	Ca2+		Sr2+		Ba2+	
	(a)	(b) Å^2	(a)	(b) Å^2	(a)	(b) Å^2
DTIMS (N2)	1	143.8	2	142.6 164.3	2	140.8 157.9
TIMS(N2)	2	129.6 136.3	5	130.8 136.6 142.2 160.8 204.5	7	124 128.2 134 138.5 158 179.3 183.4
TWIMS (V) (N2)	1	155.7	3	154.6 135.9 215.9	2	137.3 152.9
DTIMS (He)	2	67.7 77.9	3	58.9 80.9 96.2	3	58.8 77.0 84.8

Table S9. Apparent number of (a) peaks observed by IM separation and (b) their collisional cross sections, (CCS_{exp}, Å^2) for $[M+AMPA-H]^+$ where M=Mn^{2+}, Co^{2+}, Cu^{2+}, and Zn^{2+}.

M	Mn2+		Co2+		Cu2+		Zn2+	
	(a)	(b) Å^2	(a)	(b) Å^2	(a)	(b) Å^2	(a)	(b) Å^2
DTIMS (N2)	1	145.8	1	154.2	1	147.7	NA	
TIMS(N2)	NA		NA		6	124.4 129.8 137.1 143.1 150.7 156.4	3	124.3 129.5 152.3
TWIMS (V) (N2)	1	143.4	1	142.5	NA	1		145.5
DTIMS (He)		60.7	NA		7	42.7 50.1 58.4 68.7 109.5 151.2 164.2	2	47.3 70.8

DFT Energetical Orders of [M+glyphosate−H]$^{+}$ and [M+AMPA−H]$^{+}$ Isomers

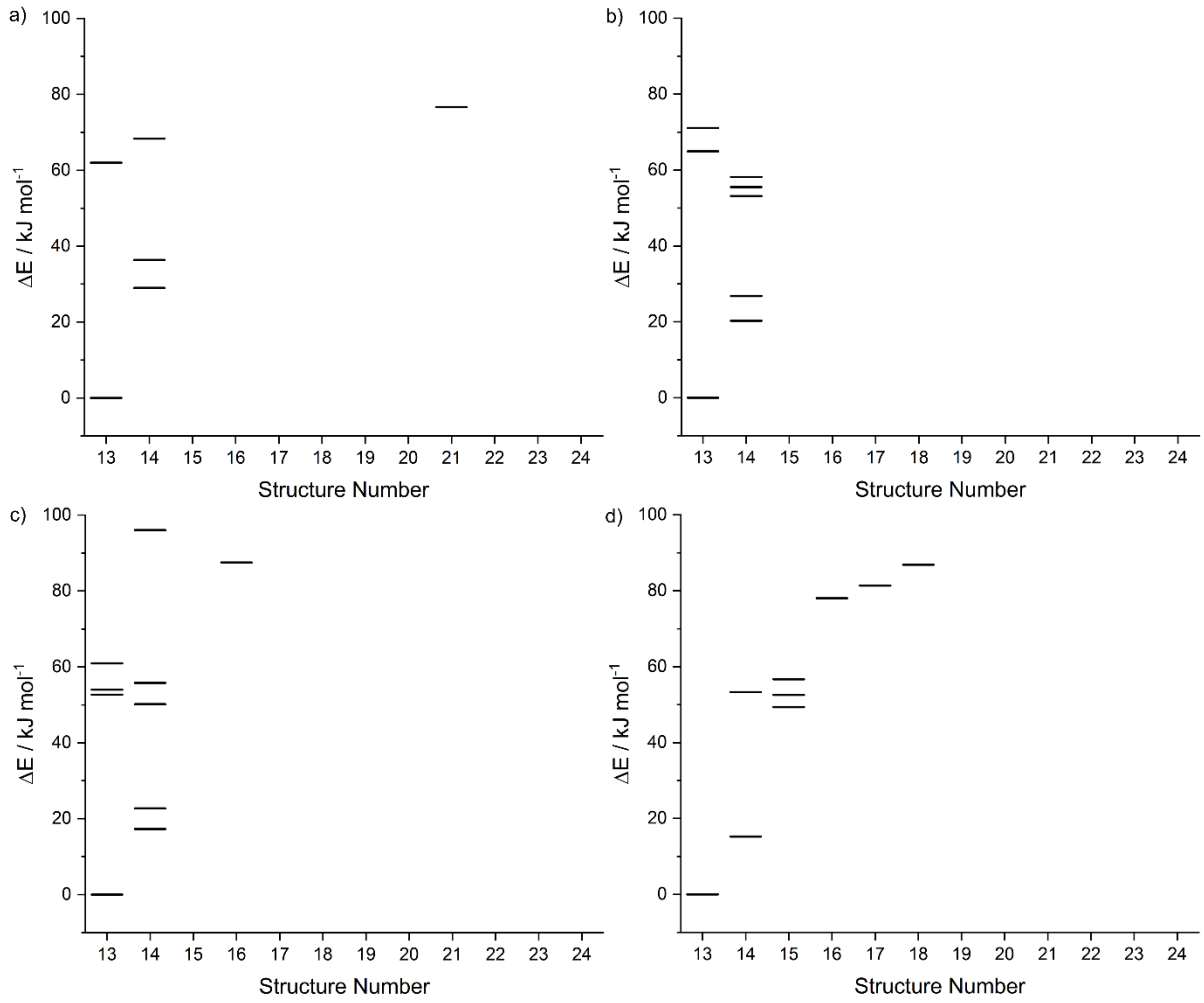

Figure S21. The energetic order for [M+glyphosate−H]$^{+}$ complexes with alkali earth metal cations where M is (a) Mg^{2+}, (b) Ca^{2+}, (c) Sr^{2+}, and (d) Ba^{2+}.

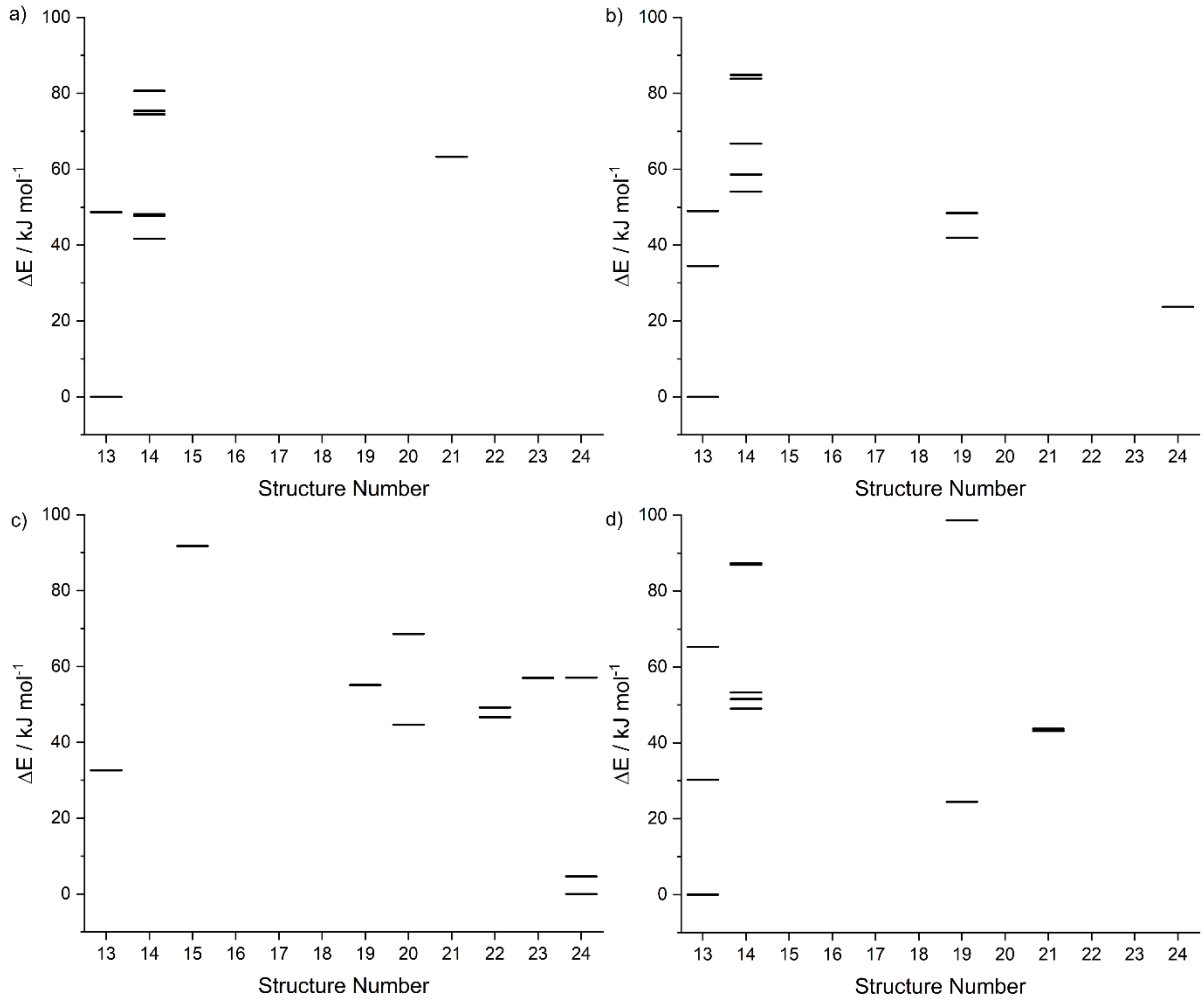

Figure S22. The energetic order for $[M+glyphosate-H]^+$ complexes with alkali earth metal cations where M is (a) Mn^{2+}, (b) Co^{2+}, (c) Cu^{2+}, and (d) Zn^{2+}.

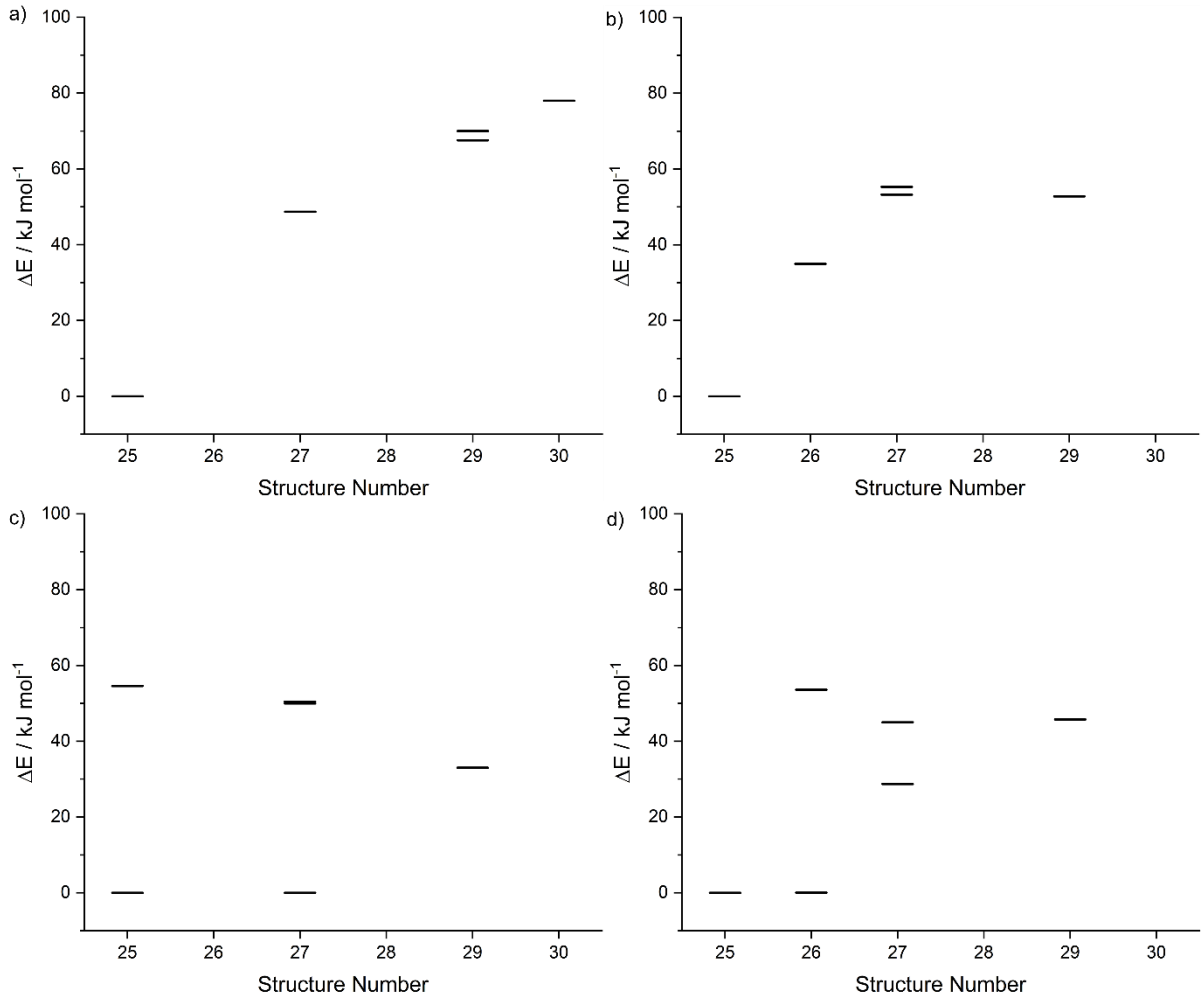

Figure S23. The energetic order for $[M+AMPA-H]^+$ complexes with alkali earth metal cations where M is (a) Mg^{2+}, (b) Ca^{2+}, (c) Sr^{2+}, and (d) Ba^{2+}.

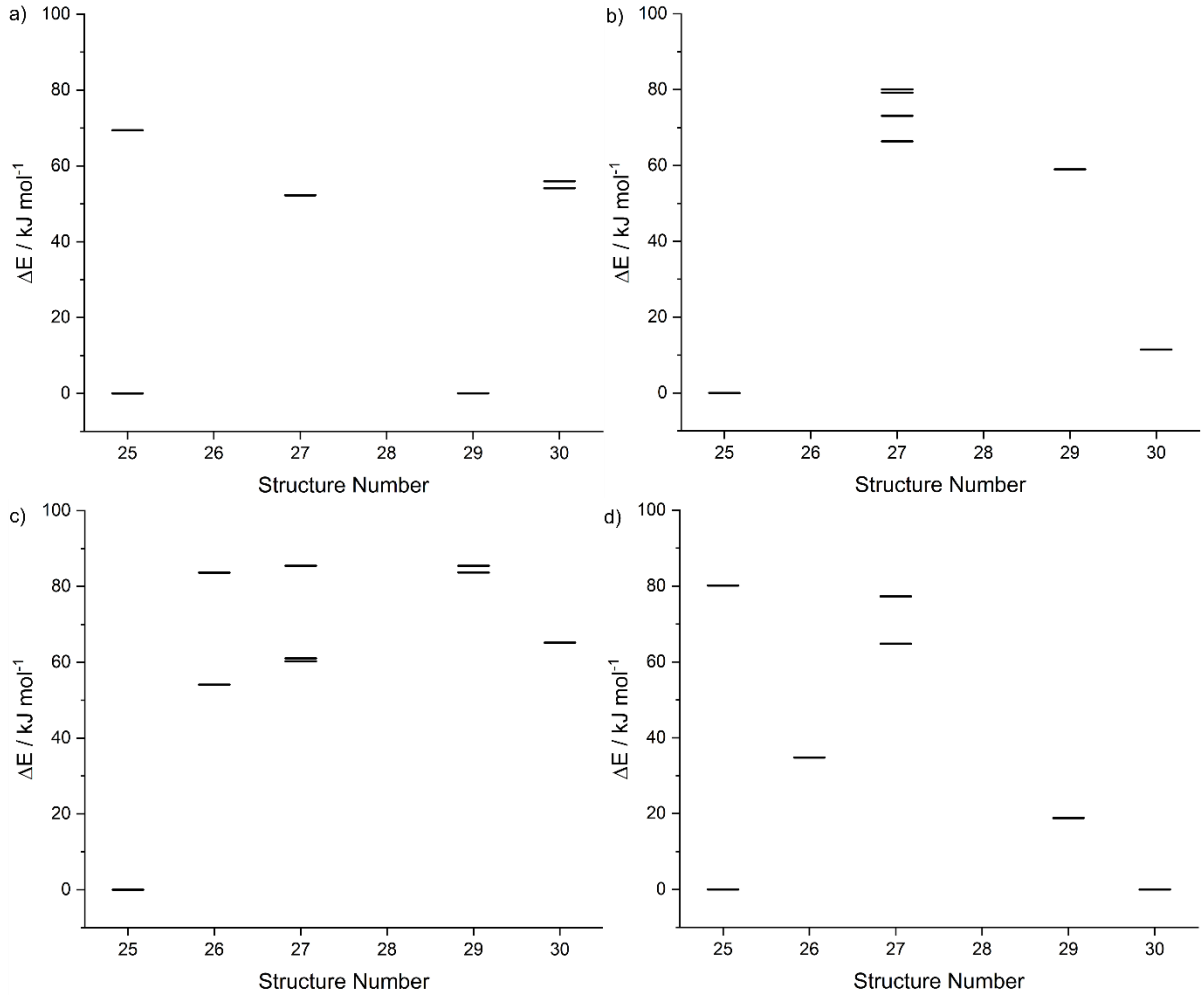

Figure S24. The energetic order for $[M+AMPA-H]^+$ complexes with alkali earth metal cations where M is (a) Mn^{2+}, (b) Co^{2+}, (c) Cu^{2+}, and (d) Zn^{2+}.

Not all $[M+glyphosate-H]^+$ complexes have 9 feasible predicted structures (Supplementary Information Figures S19-S22). When complexing with Mg^{2+}, for example, only 3 geometries were predicted to be feasible, whilst for Ba^{2+} complexes, 6 possible structural motifs were found. The structural preferences observed for $[M+glyphosate-H]^+$ with transition metal cations are completely different to alkali earth metal cations. As previously mentioned, the lowest energy structure is geometry 13, except for when complexing with Cu^{2+}. However, the structural variety of feasible structures depends on the metal. For Mn^{2+} complexes, there are only 3 structures predicted to be stable (Figure S20 a). However, Co^{2+} and Cu^{2+} while a similar ionic size to Mn^{2+}, have 4 and 7 stable predicted structures, respectively (Figure S20 b and c). While with Zn^{2+}, 4 stable isomeric structures are predicted (Figure S20 d). Of course, the cation's ionic size is not the only determining factor in the number of feasible structures, the number of electrons in their d orbitals also drives preferences. Mn^{2+} has a d^5 orbital configuration and would generally prefer square planar geometry at high spin, especially because glyphosate is a relatively small ligand and there is a lack of steric hindrance that would push for a tetrahedral geometry. A very similar structural preference distribution was observed in complexes with Zn^{2+} that has a d^{10} configuration and prefers a square planar geometry. For Co^{2+} complexes, octahedral complexes should be preferred as it has a d^7 electron configuration. However, the preference for structure number 13 is still prevalent except for its second lowest energy isomer which is structure number 24. When complexing with Cu^{2+}, there's a clear geometry preference for structures that aren't really observed in other metal complexes due to the strong preference for octahedral geometry that could be attributed to the d^9 orbital.

Like glyphosate, $[M+AMPA-H]^+$ complexes with Mg^{2+} (Figure S21 a) and Ca^{2+} (Figure S21 b) don't have many predicted stable structures. Complexes with these 2 cations have an ΔE of ~40 kJ mol^{-1} between the lowest and the second lowest energy conformers, meaning that their lowest energy conformer is much more favourable and stable. Whereas the lowest and second lowest energy conformers for Sr^{2+} (Figure S21 c) and Ba^{2+} (figure S21 d) complexes have a ΔE of less than 5 kJ $mol^{-}1$. This might be an indication that the larger cationic size of Sr^{2+} and Ba^{2+} allows them to form more types of favourable structural motifs.

The predicted $[Mn+AMPA-H]^+$ showed that there are 2 isomers that are very close in energy, despite the small ionic size of Mn^{2+} and these are geometries 25 and 29 (Figure S22 a). Interestingly, the relationship between these 2 structures is the change of deprotonation sites which indicates that there might be no preference for either deprotonation site when complexing with Mn^{2+}. Much like Mn^{2+} complexes, Zn^{2+} complexes also have competitive lowest and second lowest conformers (Figure S21 b). This is consistent with the trends observed with glyphosate complexes where complexes with Mn^{2+} and Zn^{2+} have similar behaviours which is likely contributing to their d^5 and d^{10} orbitals respectively, pushing the preference for a square planar structure. For Co^{2+} complexes, it was also observed that the second lowest energy conformer is structure number 28, like Zn^{2+} complexes. This is interesting because Co^{2+} complexes would prefer an octahedral geometry. While for Cu^{2+} complexes, the energy diagram clearly shows a very strong preference for structure number 25 as indicated by the large ΔE of more than 50 kJ mol^{-1}, again highlighting the unique Cu-N bonding.

Reported crystal structures vs DFT optimised geometries

To cross reference and benchmark the DFT optimised structures these are compared with previously reported crystal structures of the relevant complexes. For example, as previously discussed, the reported crystal structure of glyphosate calcium dihydrate shows that the metal is bonded to the phosphonate oxygen and is interacting with the other phosphonate oxygen and surrounding water molecules where the metal cation is located at the end of the glyphosate molecule instead of a central position as predicted by DFT.[12,13] For barium complex, the lowest energy DFT optimised isomer have similar bonds to the previously reported crystal structure where the Ba cation is coordinated to the phosphonate and the carboxylate site and is positioned at the centre of the molecule (Figure S25).

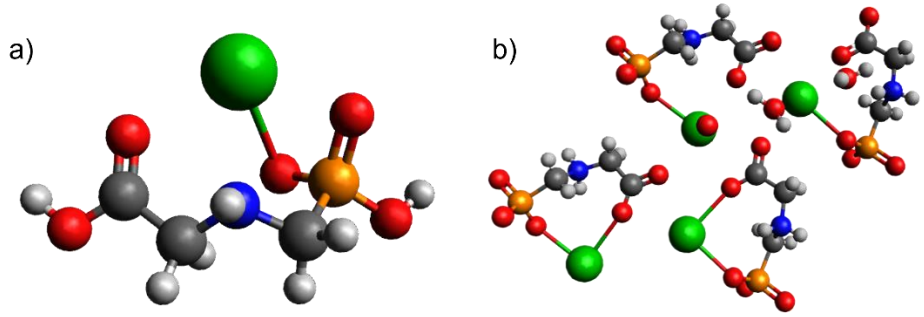

Figure S25.A comparison between (a) DFT optimised global minimum structure of $[Ba+glyphosate-H]^+$ complex and (b) reported crystal structure of glyphosate with barium.[14]

In the DFT optimised global minimum structure for glyphosate-Cu complex, the metal is bonded to the amino site. This is consistent with the previously reported crystal structure where Cu-N bond was also observed.[15] For cobalt complexes, there are two reported crystal structures by Han et al.[16] The first crystal structure show that the Co atom is bonded to the phosphonate oxygen of multiple glyphosate molecules (Figure 3 in the original publication). In the second crystal structure, the Co atom is also bonded to the phosphonate oxygen and is positioned at the end of the molecule. The same molecule also binds to another Co atom from the carboxylate end. This structure is quite similar to the DFT optimised structure **17**.

DFT optimised structures of AMPA-M complexes were also compared to reported crystal structures of the relevant complexes. For magnesium complexes, the reported crystal structure shows that the metal cation is bonded to the phosphonate oxygen.[17] The Mg atom is also bonded to three other AMPA molecules in a similar fashion and to two water molecules. This crystal structure is consistent to the DFT optimised structure **25** which is the global minimum structure. The reported crystal structure for the AMPA-Cu complex is similar to the AMPA-Mg complex which is consistent with the DFT optimised structure **25**.[18] For Zn, previously reported structure of AMPA interaction with Zn(II)-cyclen complex show that AMPA is binding with the Zn atom from the phosphonate oxygen which is also consistent with structure **25**.[19]

Importance of mass-selection in [M+glyphosate−H]$^+$ and [M+AMPA−H]$^+$ analysis

In the analysis of M+glyphosate−H]$^+$ complexes, mass-selection prior to mobility separation is crucial. The difference between mass-selected and non-mass-selected data is obvious as there are more data points in the non-mass-selected dataset (Figure S26). Not only there are more data points, the range of $^{N2}CCS_{exp}$ for the non-mass-selected data values (Figure S26 b and d) are also much larger than the one for the mass-selected data (Figure S26 a and b). The postulated reason for this observation is the fact that the larger assemblies and complexes formed by glyphosate and metals are activated and fragmented either during or after the mobility process resulting in fragments that have the same *m/z* values as the complexes that were of interest in this project. One of the tell-tale sign for this phenomenon is the 'staircase' pattern that could be observed in the IMS heatmaps. Some of the *m/z* peaks also have the same drift time as the larger complexes in with larger *m/z* which further indicates that these peaks are probably a result of fragmentation from higher-order assemblies. This post-mobility dissociation phenomenon was observed for all glyphosate-metal complexes and was also observed for AMPA-metal complexes, although to a lesser extent (Figure S27). These suspected fragment peaks can, therefore, be omitted from the analysis.

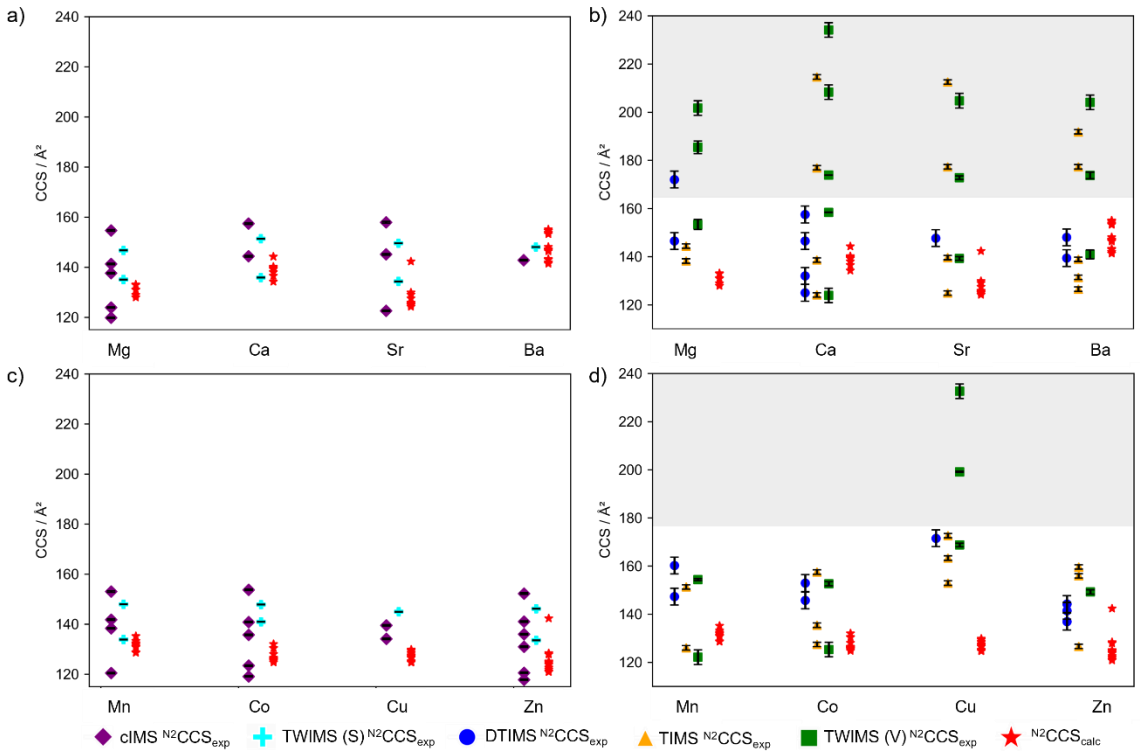

Figure S26. Cross IM-MS platforms comparison of mass-selected (a and c) and non-mass-selected (b and d) $^{N2}CCS_{exp}$ and $^{N2}CCS_{calc}$ of [M+glyphosate−H]$^+$ with alkali earth and transition metals, respectively. Peaks shaded in grey (b and d) are suspected to be results of post-mobility dissociation. Error bars represent the standard deviation.

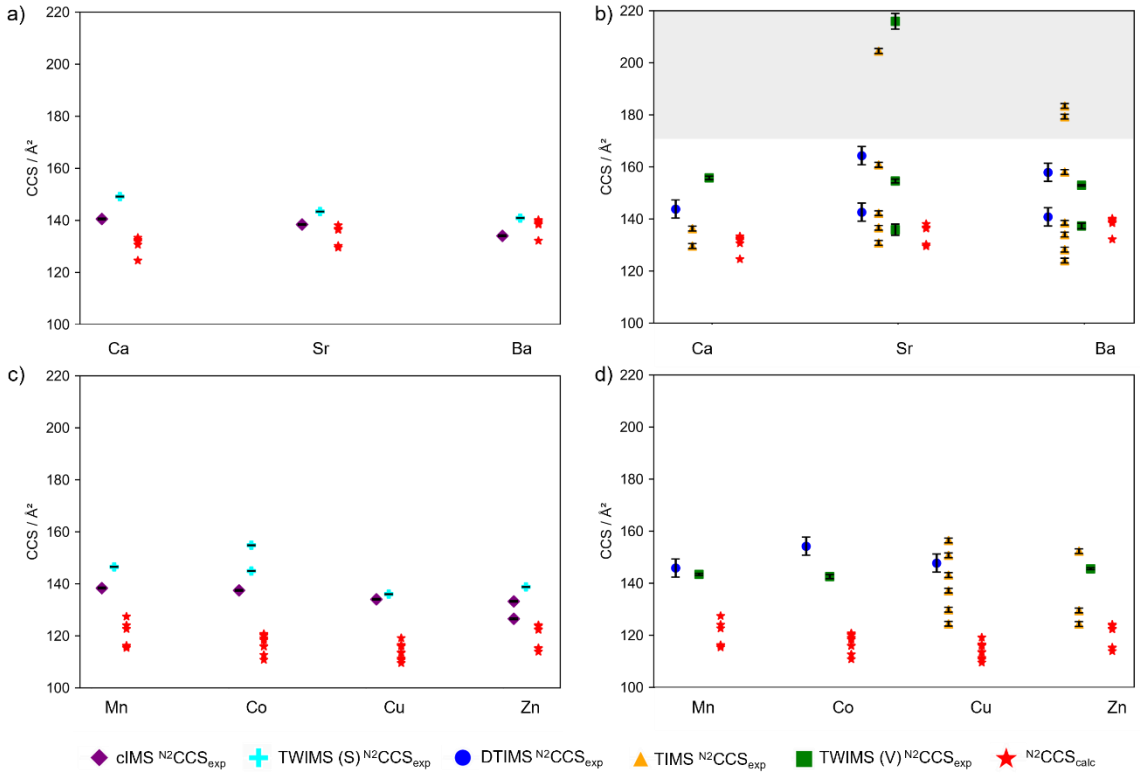

Figure S27. Cross IM-MS platforms comparison of (a and c) mass-selected and (b and d) non-mass-selected $^{N2}CCS_{exp}$ and $^{N2}CCS_{calc}$ of $[M+AMPA-H]^+$ with alkali earth and transition metals, respectively. Peaks shaded in grey (b and d) are suspected to be results of post-mobility dissociation. Error bars represent the standard deviation.

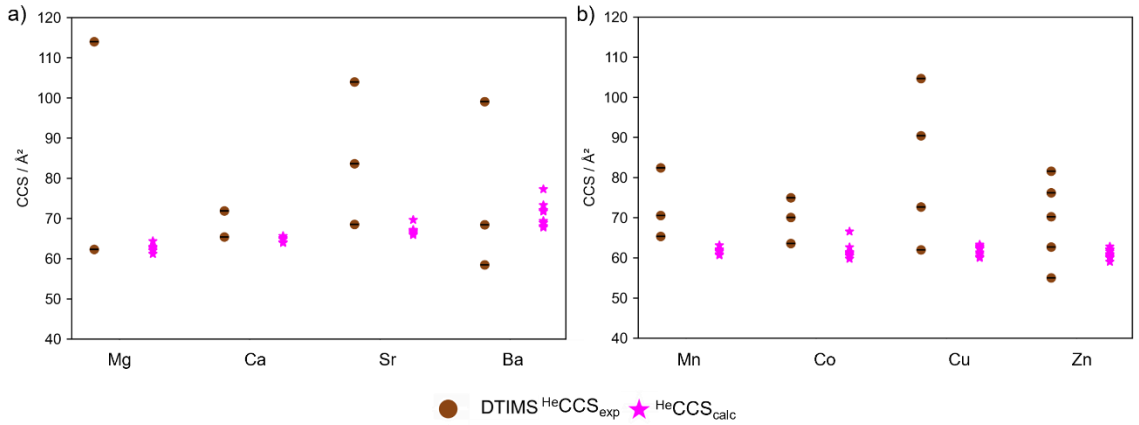

Figure S28. Comparison of non-mass-selected $^{He}CCS_{exp}$ vs $^{He}CCS_{calc}$ of $[M+glyphosate-H]^+$ with alkali earth and transition metals (a and b), respectively.

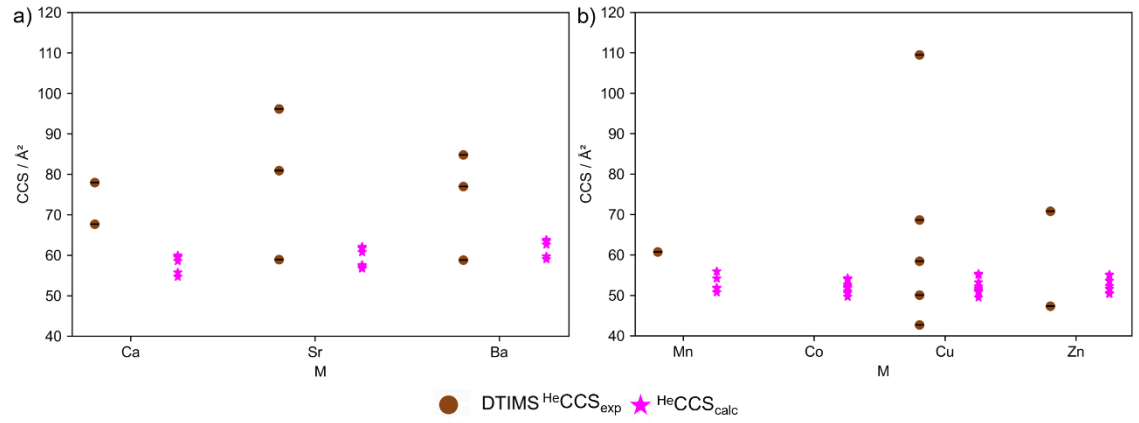

Figure S29. Comparison of non-mass-selected $^{He}CCS_{exp}$ vs $^{He}CCS_{calc}$ of $[M+AMPA-H]^+$ with alkali earth and transition metals (a and b), respectively.

It was mentioned previously that the agreement between $^{He}CCS_{exp}$ and $^{He}CCS_{calc}$ for $[M+glyphosate-H]^+$ complexes are better than the equivalent comparison in N_2. However, $[M+AMPA-H]^+$ complexes, this is not the case. Comparison of $^{He}CCS_{exp}$ for the most abundant peak and $^{He}CCS_{calc}$ for the lowest energy conformers don't agree very well with differences of 21%, 3.8%, and 0.4% for Ca, Sr and Ba respectively. For Mn, Cu and Zn, the differences were 17.9%, 15.9%, and 6.6% respectively. The large percentage of difference is interesting and could be attributed to a combination of low signal intensity in the experiments and that some $^{He}CCS_{exp}$ values agree with $HeCCS_{calc}$ value that is not the lowest energy conformer. For example, the most abundant $^{He}CCS_{exp}$ for $[Sr+AMPA-H]^+$ is 58.9 Å² which has a 2.3% difference when compared to the $^{He}CCS_{calc}$ (57.6 Å²) of the 3rd lowest energy isomer predicted for the complex.

IM-IRMPD-MS of [Ba+glyphosate-H]$^+$

Since IM-MS results alone weren't sufficient to conclusively characterise the structure of [Ba+glyphosate-H]$^+$ complex, the experiment was repeated on a custom instrument combining IM-MS and IRMPD (Experimental Methods, page S5).[7] Experimentally obtained IR spectrum of the mass- and mobility-selected [Ba+glyphosate-H]$^+$ complex was then compared to the predicted IR spectra for a variety of [Ba+glyphosate-H]$^+$ structures. When overlaid, the experimental spectrum and the predicted spectrum of the global minimum structure showed strong agreement, confirming that the experimentally observed structure corresponds to the global minimum (Figure S30). In contrast, a comparison between the experimental spectrum and the predicted spectrum of the second lowest-energy geometry of [Ba+glyphosate-H]$^+$ revealed a poor match (Figure S31). This further supports our findings that the gas phase structure of [Ba+glyphosate-H]$^+$ observed experimentally is one where the metal cation is bonded to the deprotonated phosphonate group and the metal is located at the centre of the glyphosate molecule to maximise interaction with the electron rich groups.

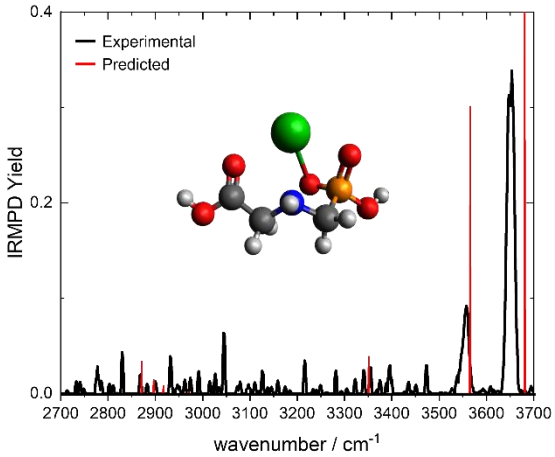

Figure S30. Overlay of experimental (black) and predicted (red, scaled by 0.95) spectra for the global minimum structure of [Ba+glyphosate-H]$^+$.

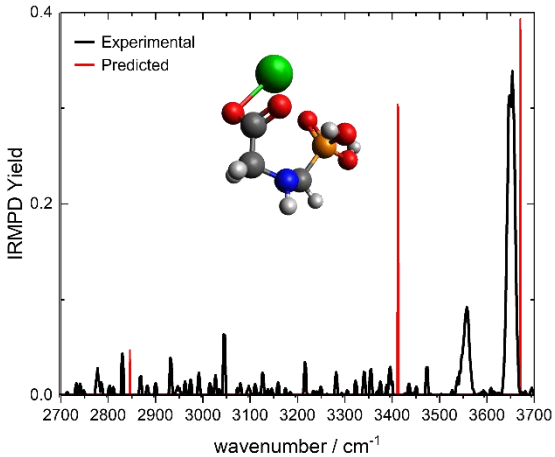

Figure S31. Overlay of experimental (black) and predicted (red, scaled by 0.95) spectra for the second lowest energy structure (ΔE = 15 kJ mol^{-1}) of [Ba+glyphosate-H]$^+$

Polyalanine Calibration for TWIMS (Synapt) in N_2

The CCS_{exp} values obtained from the TWIMS (Synapt) platform in N_2 was obtained from a calibration curve using a polyalanine as the calibrant using methods as previously described in Thalassinos et al.[3] Previously reported polyalanine CCS values by Bush et al.[6] were plotted in the form of CCS' against dt'.

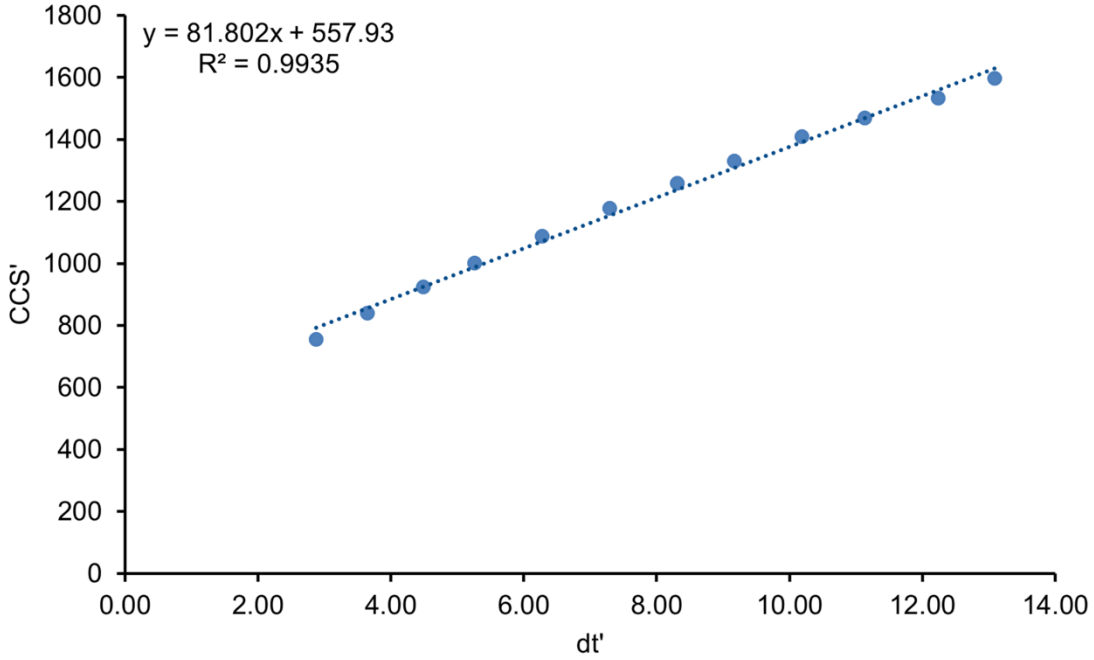

Figure S32. Calibration curve for determining the $^{N2}CCS_{exp}$ values of samples measured on the TWIMS (Synapt) platform.

Polyalanine Calibration for DTIMS in He

The CCS_{exp} values obtained from the DTIMS in He was obtained from manual calibration using polyalanine as the calibrant. The drift time of the measured polyalanine ions were used to plot a calibration curve against previously reported values by Bush et al.[6]

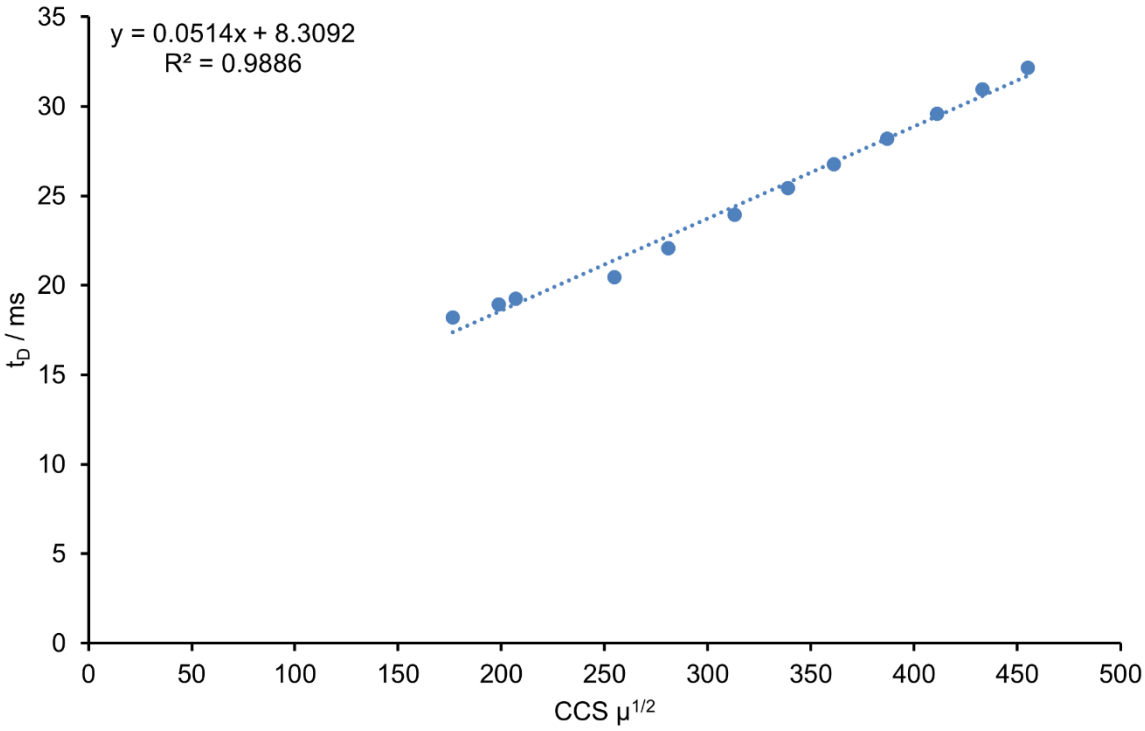

Figure S33. Calibration curve for determining the CCS_{exp} values of samples measured on the DTIMS.

References

1 N. J. Rijs, T. Weiske, M. Schlangen and H. Schwarz, *Anal. Chem.*, 2015, **87**, 9769–9776.
2 N. J. Rijs, T. Weiske, M. Schlangen and H. Schwarz, *Anal. Chem.*, 2015, **87**, 11601–11601.
3 K. Thalassinos, M. Grabenauer, S. E. Slade, G. R. Hilton, M. T. Bowers and J. H. Scrivens, *Anal. Chem.*, 2009, **81**, 248–254.
4 F. Hennrich, S. Ito, P. Weis, M. Neumaier, S. Takano, T. Tsukuda and M. M. Kappes, *Phys. Chem. Chem. Phys.*, 2024, **26**, 8408–8418.
5 H. E. Revercomb and E. A. Mason, *Anal. Chem.*, 1975, **47**, 970–983.
6 M. F. Bush, I. D. G. Campuzano and C. V. Robinson, *Anal. Chem.*, 2012, **84**, 7124–7130.
7 S. Bakels, S. Daly, B. Doğan, M. Baerenfaenger, J. Commandeur and A. M. Rijs, *Anal. Chem.*, 2024, **96**, 34, 13962-13970.
8 Y. Zhao and D. G. Truhlar, *Theor. Chem. Acc.*, 2008, **120**, 215–241.
9 F. Weigend and R. Ahlrichs, *Phys. Chem. Chem. Phys.*, 2005, **7**, 3297–3305.
10 F. Weigend, *Phys. Chem. Chem. Phys.*, 2006, **8**, 1057–1065.
11 F. F. Nielson, S. M. Colby, D. G. Thomas, R. S. Renslow and T. O. Metz, *Anal. Chem.*, 2021, **93**, 3830–3838.
12 P. H. Smith and K. N. Raymond, *Inorg. Chem.*, 1988, **27**, 1056–1061.
13 P. R. Rudolf, E. T. Clarke, A. E. Martell and A. Clearfield, *Acta Cryst C*, 1988, **44**, 796–799.
14 D. S. Sagatys, C. Dahlgren, G. Smith, R. C. Bott and A. C. Willis, *Aust. J. Chem.*, 2000, **53**, 77–81.
15 E. T. Clarke, P. R. Rudolf, A. E. Martell and A. Clearfield, *Inorganica Chim. Acta*, 1989, **164**, 59–63.
16 G.-F. Han, H.-Z. Luo, Q. Ye and R.-G. Xiong, *ZAAC*, 2008, **634**, 1991–1995.
17 M. Lutz and G. Mueller, *Inorg. Chim. Acta*, 1995, **232**, 189.
18 T. Glowiak, W. Sawka-Dobrowolska, B. Jezowska-Trzebiatowska and A. Antonow, *J. Cryst. Mol. Struct.*, 1980, **10**, 1–10.
19 I. Rostasova, M. Vilkova, Z. Vargova, R. Gyepes, M. Litecka, V. Kubicek, J. Imrich and I. Lukes, *New J. Chem.*, 2017, **41**, 7253–7259.